Spin-charge conversion in a multiterminal Aharonov-Casher ring coupled to precessing ferromagnets: A charge-conserving Floquet nonequilibrium Green function approach

Son-Hsien Chen (陳松賢),* Chien-Liang Chen, and Ching-Ray Chang (張慶瑞)†
Department of Physics, National Taiwan University, Taipei 10617, Taiwan

Farzad Mahfouzi
Department of Physics and Astronomy, University of Delaware, Newark, Delaware 19716-2570, USA
(Received 25 July 2012; published 2 January 2013)

We derive a nonperturbative solution to the Floquet nonequilibrium Green function (Floquet NEGF) describing open quantum systems periodically driven by an external field of arbitrary strength of frequency. By adopting the reduced-zone scheme, we obtain expressions rendering conserved charge currents for *any given maximum number of photons*, distinguishable from other existing Floquet-NEGF-based expressions where, less feasibly, an infinite number of photons needs to be taken into account to ensure the conservation. To justify our derived formalism and to investigate spin-charge conversions by spin-orbit coupling (SOC), we consider the spin-driven setups as reciprocal to the electric-driven setups in Souma and Nikolić [Phys. Rev. B **70**, 195346 (2004); Phys. Rev. Lett. **94**, 106602 (2005)]. In our setups, *pure* spin currents are driven by the magnetization dynamics of a precessing ferromagnetic (FM) island and then are pumped into the adjacent two- or four-terminal mesoscopic Aharonov-Casher (AC) ring of Rashba SOC where spin-charge conversions take place. Our spin-driven results show reciprocal features that excellently agree with the findings in the electric-driven setups mentioned above. We propose two types of symmetry operations, under which the AC ring Hamiltonian is invariant, to argue the relations of the pumped/converted currents in the leads within the same or between different pumping configurations. The symmetry arguments are independent of the ring width and the number of open channels in the leads, terminals, and precessing FM islands. In particular, *net* pure in-plane spin currents and pure spin currents can be generated in the leads for certain setups of two terminals and two precessing FM islands with the current magnitude and polarization direction tunable by the pumping configuration, gate voltage covering the two-terminal AC ring in between the FM islands.

DOI: 10.1103/PhysRevB.87.045402 PACS number(s): 72.25.Dc, 03.65.Vf, 85.75.−d, 72.10.Bg

I. INTRODUCTION

Spin, one form of angular momentum, is a vector distinguishing from the scaler charge and thus provides more degrees of freedom than the conventional charge for people to utilize in signal-storage and signal-transfer devices; particularly, the investigation on manipulating and comprehending the electron spins, termed spintronics, has become an emerging field due to its potential industry applications.[1–4] A key physical quantity in spintronics is the spin current, while there are no direct measurements such as "spin current ammeter" to detect the spin current.[5] In this paper, we propose a setup that takes advantages of the inverse spin-Hall effect (ISHE) and the Aharonov-Casher (AC) effect to convert the pumped spin currents by precessing magnetization of a ferromagnetic (FM) island into more accessibly measurable charge currents.

In the spin-Hall effect (SHE), a longitudinal injection of a conventional unpolarized charge current into a system with either extrinsic (due to impurities)[6,7] or intrinsic (due to band structure)[8,9] spin-orbit coupling (SOC) generates a transverse *pure* spin current in the four-terminal geometry or the corresponding spin accumulation along the lateral edges in the two-terminal geometry. While the magnitude of the pure spin current generated by SHE in metals and semiconductors is rather small and difficult to control,[4] the ISHE[7,10] has recently emerged as the principal experimental tool to detect induction of pure spin currents by different sources. In the ISHE (which can be viewed[7,10] as the Onsager reciprocal phenomenon of the direct SHE), a longitudinal spin current generates a transverse charge current or voltage in an open circuit. Experimental examples employing ISHE to detect pure spin current include (i) a pure spin current pumped by precessing magnetization of a single FM layer under ferromagnetic resonance (FMR) conditions with detection by injecting the pumped current into an adjacent normal-metal (NM), such as Pt, Pd, Au, and Mo, or semiconductor layer;[11,12] (ii) spin currents generated in nonlocal spin valves;[13] (iii) a transient ballistic pure spin current injected[14] by a pair of laser pulses in GaAs multiple quantum wells being converted into a charge current generated by ISHE before the first electron-hole scattering event, thereby providing unambiguous evidence for the intrinsic direct and inverse SHE.

Spin pumping[15] by precessing magnetization is a phenomenon where the moving magnetization of a single FM layer, driven by microwave radiation under the FMR, emits spin current into adjacent NM layers. The emitted spin current is pure in the sense that it is not accompanied by any net charge flux. This effect is termed pumping because it occurs in the absence of any dc bias voltage. Particularly, the detection of pure spin currents pumped by magnetization dynamics has become a widely employed technique[12] to characterize the effectiveness of the charge-spin conversion by the SHE via measuring the material-specific spin-Hall angle (i.e., the ratio of spin-Hall and charge conductivities). The same ISHE-based technique is almost exclusively used in the very recent observations of thermal spin pumping and magnon-phonon-mediated spin-Seebeck effect.[16] Also, spin pumping makes it possible

to inject[17] spins into semiconductors with electrically tunable efficiency across an Ohmic contact, evading the notorious problem[18] of impedance mismatch between the FM conductor and high-resistivity material.

On the theoretical side, the mechanisms for converting pumped pure spin current into charge current, due to a region with intrinsic or extrinsic SOC into which the pumped spin current is injected, have been analyzed in a number of recent studies. For example, Ref. 19 has shown that both transverse and longitudinal charge currents are generated in the four-terminal Rashba-spin-split two-dimensional electron gas (2DEG) of square shape which is adjacent to the FM island with precessing magnetization that pumps longitudinal pure spin current into the 2DEG. In this scheme, the output charge current can be increased by increasing the strength of the Rashba SOC in the 2DEG.

Furthermore, the recent alternative description[20] of spin pumping in FM|NM multilayers, which encompasses both the earlier considered[21] nonlocal diffusion of the spin accumulation at the FM|NM interface generated by magnetization precession and the effective field described by the "standard model"[15] of spin pumping viewed as an example of adiabatic quantum pumping that is captured by the Brouwer scattering formula,[22] has shown that *spin-charge conversion* does not always occur and that the conversion depends sensitively on the type of spin-orbit interactions. That is, unlike in FM|NM systems where spin-charge conversion is driven by the extrinsic SOC and assumed to follow simple phenomenological prediction $\mathbf{j}_c \propto \mathbf{S} \times \mathbf{j}_s$ ($\mathbf{j}_c$ is charge current density, $\mathbf{S}$ is the spin polarization direction, and $\mathbf{j}_s$ is the injected spin current density), the pumped charge currents in Rashba systems were found to deviate from this naive formula.

Thus, the whole phenomenon of spin-charge conversion after pure spin current is injected into a system with SOC needs to be discussed together with the origin of spin currents and the type of SOC employed for the conversion.[20] Here we analyze spin current generation by one or two precessing FM islands and the corresponding spin-charge conversion in two- and four-terminal mesoscopic rings, adjacent to those islands and patterned in the 2DEG with the Rashba SOC. Unlike the spin-charge conversion in experimental and theoretical studies discussed above, where electronic transport occurs in semiclassical nature,[20] the device depicted in Fig. 1 involves spin-sensitive quantum-interference effects caused by the difference in the AC phase[23–25] gained by a spin traveling around the *phase-coherent* ring. The AC effect,[23–25] in which magnetic dipoles travel around a tube of electric charge, can be regarded as a special case of a geometric phase. For typical ring sizes and strengths of Rashba SOC in InAlAs/InGaAs heterostructures, the AC phase acquired by a (spin) magnetic moment moving in the presence of an electrical field is of Aharonov-Anandan[26] (rather than Berry) type due to the fact that the electron spin cannot[25] adiabatically maintain a fixed orientation with respect to the radial effective (momentum-dependent and, therefore, inhomogeneous) magnetic field associated with the Rashba SOC. In fact, the AC phase for spins traveling around the mesoscopic ring consists of not only the geometric phase, but also a dynamical phase arising from the additional spin precession driven by the local effective magnetic field.[27]

Accordingly, giving electrons such geometric phase makes it possible to manipulate the magnitude of charge and spin

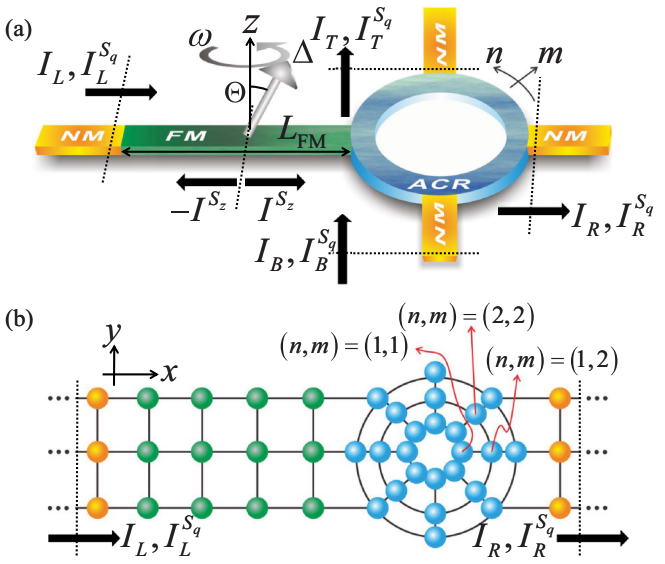

FIG. 1. (Color online) Schematics of the (a) four- and (b) two-terminal device setups. A precessing ferromagnetic (FM) island driven by microwaves pumps pure spin current into the Aharonov-Casher (AC) ring (where the spin-charge conversion takes place) patterned within a two-dimensional electron gas in the x-y plane with the Rashba spin-orbit coupling. The semi-infinite normal-metal (NM) leads, in the absence of any dc bias voltage, are attached to the AC ring to probe the output time-averaged (over a precession period) pumped charge (spin-q with $q \in \{x,y,z\}$) currents, I_L ($I_L^{S_q}$), I_B ($I_B^{S_q}$), I_R ($I_R^{S_q}$), and I_T ($I_T^{S_q}$), in the left, bottom, right, and top of the device, respectively. The FM island is of length $L_{\rm FM}$, and exchange splitting Δ. The magnetization of the FM precesses around the z axis with frequency ω and cone angle Θ . The AC ring lattice sites along the tangential and normal directions are denoted by n and m, respectively.

currents in AC rings due to the fact that, unlike the usual case of intrinsically fixed phases, the ring experiments allow one to steer geometric phases in a controlled way through the system geometry and other various tunable parameters.[28] For example, the destructive quantum interferences, controlled by the accumulated AC phase via tuning of the strength of the Rashba SOC (which depends on the applied top-gate voltage),[29,30] cause unpolarized charge current injected into the two-terminal AC rings to diminish[27,28,31–34] [to zero[34] if the ring is strictly one-dimensional (1D)]. Similarly, in four-terminal AC rings one encounters quantum-interference-controlled SHE, predicted in Ref. 35 and extended to different types of SOC and ring geometry in Refs. 36 and 37, where spin-Hall conductance can be tuned from zero to a finite value of the order of spin conductance quantum $e/4\pi$.

The goal of this study is threefold: (i) to provide a unified microscopic quantum transport theory based on the nonperturbative solution of the time-dependent nonequilibrium Green function (NEGF) in the Floquet representation[38] which *conserves charge current at each level of approximation* (i.e., number of microwave photons taken into account depending on the strength of the driving field) for both the spin current generation by the magnetization dynamics and spin-charge conversion in the adjacent region with SOC; (ii) to understand

how output spin and charge currents from multiterminal AC ring devices (such as in Fig. 1) can be controlled by the top-gate covering the ring, by the cone angle of precessing magnetization set by the input microwave power driving the precession, and by the setup geometry; (iii) to examine whether the device setup in Fig. 1 can be used as a new playground for experiments[25,28,31,32] measuring charge currents to detect quantum interference effects involving AC phase in a single mesoscopic ring where multichannel effects in a typical ring of finite width act as effective dephasing (by entangling spin and orbital degrees of freedom[39] or averaging over orbital channels with different interference patterns),[34] thereby randomizing interference patterns as in conventional measurements using dc bias voltage.[31]

The paper is organized as follows. In Sec. II, we specify our pumping device and the adopted Hamiltonian. Section III formulates the solution to the Floquet-NEGF equations. Our numerical results are discussed in Sec. IV according to the chosen parameters and units given in Sec. IV A. In Sec. IV B, we examine both the pumped charge and spin currents responsible for the AC phase and ISHE effects and driven by spin pumping in the *absence* of any dc bias voltage, i.e., the spin-driven setups as the counterparts to the conventional voltage-bias driven (electric-driven) setups with two-terminal[27,33,34] and four-terminal[35] mesoscopic AC rings of the Rashba SOC. Section IV D illustrates different pumping symmetries of the AC ring. We conclude in Sec. V. We also add an appendix to show how charge current can be conserved in our present work and to compare our derived expression of the current with other existing formulas.

Our key results are as follows: (i) To arrive at Eqs. (32)–(35), we solve the Floquet-NEGF equations and use the so-called reduced-zone scheme[38] which guarantees conservation of charge currents for any given maximum number of photons (as shown in the Appendix), unlike other recent approaches based on continued-fraction solutions[40–43] where charge conservation is ensured only in the limit of infinite number of photons. (ii) With Fig. 2 through Fig. 7, we analyze the pumped currents in the spin-driven setup Fig. 1. The results are in good correspondence with the reciprocal electric-driven results shown in Refs. 34 and 35, justifying the derived formalism herein. Detail examinations, based on the AC effect and ISHE, of the modulations of both the pumped charge and spin currents are given. (iii) In Sec. IV D, we tailor the pumping symmetry under which the Hamiltonian of the AC ring of Rashba SOC remains invariant. By performing the symmetry operations on one specific pumping configuration, we can obtain the relations between pumped currents in the same or different pumping configurations (or setup geometry). Although we illustrate the symmetry operations by considering only the setups of two-terminal two-precessing FM islands, the symmetry arguments are applicable to the case of an arbitrary number of terminals and FM islands as well, giving multifarious manipulations of the pumped currents via setup geometry. In particular, Figs. 10, 11, and Figs. 14–17 show that the pumped spin currents are pure and are of magnitude and polarization direction tunable by the top-gate voltage controlling the strength of the Rashba SOC and by the pumping configurations.

II. DEVICE SETUP AND HAMILTONIAN

Consider the spin-driven four-terminal (or four-lead) setup in Fig. 1(a). A ferromagnet, FM, with precession axis along the z direction, contacts the AC ring of Rashba SOC in the x-y plane from the left. The FM plays the role of a spin-z source, pumping pure spin-z currents into the ring via the FM|AC-ring interface. The spin-charge conversion takes place in the AC ring. The pumped or converted charge current I_p and spin current $I_p^{S_q}$ are probed by the NM leads where currents are conserved with $p = L, R, B$, and T indicating the currents flowing through the left, right, bottom, and top leads and $q \in \{x, y, z\}$ standing for the pumped spin-x, y, and z currents, respectively.

All computed pumped spin and charge currents are time averaged (over one precession period); they carry positive signs if the flow direction is in the $+x$ or $+y$ direction or minus if flow direction is in the $-x$ or $-y$. In the two-terminal setup, Fig. 1(b), we have two NMs labeled by $p = L, R$. Note that, except for the number of leads, Fig. 1(b) does not differ from Fig. 1(a), but just further shows the lattice structure of the device. The AC ring is modeled by $m = 1 \cdots M$ concentric circles of the same number of lattice sites, and in a circle m the lattice sites are indexed by $n = 1 \cdots N$. For instance, we have $(M, N) = (3, 8)$ in Fig. 1(b). The NMs and the FM are modeled by square lattices, while each NM is of semi-infinite length, and the FM is of finite length, namely, an island.

The Hamiltonian of the whole device can be divided into six terms,

$$H(t) = H_{\rm ACR} + H_{\rm NM} + H_{\rm FM}(t) + H_{\text{NM-ACR}} + H_{\text{FM-ACR}} + H_{\text{FM-NM}}, \quad (1)$$

where $H_{\rm ACR}$, $H_{\rm NM}$, and $H_{\rm FM}$ account for the Hamiltonian of the AC ring, NM, and FM, respectively. The term $H_{\text{NM-ACR}}$ describes the hybridization between NMs and the AC ring, and $H_{\text{FM-ACR}}$ ($H_{\text{FM-NM}}$), the hybridization between FM and the AC ring (FM and NMs). Note that the time-dependent Hamiltonian originates only from the precessing FM, $H_{\rm FM}(t)$. Below, we express these six terms explicitly.

Focus on $H_{\rm ACR}$ first. As given in Ref. 34, the ring Hamiltonian can be written as

$$H_{\rm ACR} = \Bigg[\sum_{\sigma,\sigma'=\uparrow,\downarrow} \varepsilon^{n,m} \hat{a}^\dagger_{n,m;\sigma} \hat{a}_{n,m;\sigma} - \Bigg(\sum_{n=1}^{N} \sum_{m=1}^{M} \gamma_\phi^{n,n+1,m;\sigma,\sigma'} \hat{a}^\dagger_{n,m;\sigma} \hat{a}_{n+1,m;\sigma'} - \sum_{n=1}^{N} \sum_{m=1}^{M-1} \gamma_r^{m,m+1,n;\sigma,\sigma'} \hat{a}^\dagger_{n,m;\sigma} \hat{a}_{n,m+1;\sigma'} \Bigg) \Bigg] + \text{H.c.}, \quad (2)$$

with n and m denoting the lattice sites along the tangential (ϕ) and normal (r) directions as illustrated in Fig. 1(b), respectively. The creation (annihilation) operator at site (n,m) of spin σ is $\hat{a}^\dagger_{n,m;\sigma}$ ($\hat{a}_{n,m;\sigma}$). The on-site potential $\varepsilon^{n,m}$ at site (n,m) takes into account the disorder and can be tuned by applying a top-gate voltage. In what follows, unless further specified, we will assume that the AC ring, NM, and FM are all clean conductors, i.e., of zero on-site potentials. The

hopping along the ϕ direction,

$$\gamma_{\phi}^{n,n+1,m} = \frac{1}{(r_m/a)^2\Delta\phi^2}\gamma_0 I_s - i\frac{\gamma_{\rm SO}}{(r_m/a)\Delta\phi} \times(\sigma_x\cos\phi_{n,n+1} + \sigma_y\sin\phi_{n,n+1}), \quad (3)$$

and along the r direction,

$$\gamma_r^{m,m+1,n} = \gamma_0 I_s + i\gamma_{\rm SO}(\sigma_y\cos\phi_n - \sigma_x\sin\phi_n), \quad (4)$$

consists of two terms proportional to γ_0 that originates from the kinetic energy and to $\gamma_{\rm SO}$ that results from the Rashba SOC, with $\phi_n \equiv 2\pi(n-1)/N$, $\phi_{n,n+1} \equiv (\phi_n+\phi_{n+1})/2$, $\Delta\phi = \phi_2 - \phi_1$, $r_m \equiv r_1 + (m-1)a$, $\gamma_0 = \hbar(2ma^2)^{-1}$, $\gamma_{\rm SO} = \alpha(2a)^{-1}$, a being the lattice spacing, $\sigma_q = S_q 2/\hbar$ being the Pauli matrices, and $\hbar \times 2\pi$, the Planck constant. It is worth addressing that the Hamiltonian (2) yields the same spin precession as obtained by the SU(2) non-Abelian spin-orbit gauge[44] that absorbs the Rashba SOC term for the U-shaped[45] 1D conductor; furthermore, the above form of the concentric tight-binding Hamiltonian was also used to theoretically model the Rashba SOC in HgTe/HgCdTe quantum wells in Ref. 31, showing experimental observations of the AC effect in good agreements with the theoretical predictions, and thus strengthening the validity of the ring Hamiltonian Eq. (2).

The currents are probed by the un-biased NM leads whose Hamiltonian reads

$$H_{\rm NM} = -\sum_{p}\sum_{\sigma=\uparrow,\downarrow}\sum_{\langle\mu,\mu'\rangle}\gamma_0\hat{b}^{(p)\dagger}_{\mu;\sigma}\hat{b}^{(p)}_{\mu';\sigma}, \quad (5)$$

where $\hat{b}^{(p)\dagger}_{\mu;\sigma}$ is the creation operator and $\hat{b}^{(p)}_{\mu;\sigma}$ is the annihilation operator in lead p at site μ of spin σ. The pure spin currents are pumped by the precessing FM described by

$$\begin{aligned} H_{\rm FM}(t) &= \sum_{\sigma,\sigma'=\uparrow,\downarrow}\sum_{\nu}\frac{\Delta}{2}\vec{M}(t)\cdot\vec{\sigma}\hat{c}^{\dagger}_{\nu;\sigma}\hat{c}_{\nu;\sigma'} \\ &\quad - \sum_{\sigma=\uparrow,\downarrow}\sum_{\langle\nu,\nu'\rangle}\gamma_0\hat{c}^{\dagger}_{\nu;\sigma}\hat{c}_{\nu';\sigma} \\ &= \sum_{\sigma,\sigma'=\uparrow,\downarrow}\sum_{\nu}\Big[Ve^{i(\omega t+\Phi)} + V^{\dagger}e^{-i(\omega t+\Phi)} \\ &\quad + \frac{\Delta}{2}\cos\Theta\sigma_z\Big]\hat{c}^{\dagger}_{\nu;\sigma}\hat{c}_{\nu';\sigma'} \\ &\quad - \sum_{\sigma=\uparrow,\downarrow}\sum_{\langle\nu,\nu'\rangle}\gamma_0\hat{c}^{\dagger}_{\nu;\sigma}\hat{c}_{\nu';\sigma}, \end{aligned} \quad (6)$$

with $\vec{M}(t) = [\sin\Theta\cos(\omega t+\Phi), \sin\theta\sin(\omega t+\Phi), \cos\Theta]$ giving $V = \sin\Theta(\sigma_x - i\sigma_y)\Delta/4$. The $\hat{c}^{\dagger}_{\nu;\sigma}$ $(\hat{c}_{\nu;\sigma})$ is the creation (annihilation) operator at site ν in the FM of spin σ. The hybridizations between adjacent materials,

$$H_{\rm NM\text{-}ACR} = -\gamma_0\sum_{p}\sum_{\sigma=\uparrow,\downarrow}\sum_{\langle\mu,n\rangle}\hat{b}^{\dagger}_{p;i;\sigma}\hat{a}_{n;\sigma} + \text{H.c.},$$

$$H_{\rm FM\text{-}ACR} = -\gamma_0\sum_{\sigma=\uparrow,\downarrow}\sum_{\langle\nu,n\rangle}\hat{c}^{\dagger}_{j;\sigma}\hat{a}_{n;\sigma} + \text{H.c.},$$

and

$$H_{\rm FM\text{-}NM} = -\gamma_0\sum_{p}\sum_{\sigma=\uparrow,\downarrow}\sum_{\langle\nu,\mu\rangle}\hat{c}^{\dagger}_{j;\sigma}\hat{b}_{j;i;\sigma} + \text{H.c.},$$

are set to be of the same strength, namely, γ_0.

III. FLOQUET NONEQUILIBRIUM GREEN FUNCTION APPROACH FOR PERIODICALLY DRIVEN OPEN QUANTUM SYSTEMS

In the devices where spin flip or spin precession is absent, the problem of spin pumping by magnetization dynamics can be greatly simplified by mapping it onto a time-independent one in the frame rotating with the precessing magnetization.[46–49] However, the device in Fig. 1 contains Rashba SOC which causes spin-up to evolve into to spin-down by spin precession, so that the device Hamiltonian transformed in the rotating frame contains time-dependent SOC terms.

In the adiabatic regime $\omega \to 0$, which is satisfied for pumping by magnetization dynamics since the energy of microwave photons $\hbar\omega$ is much smaller than other relevant energy scales,[50] one can employ the Brouwer scattering formula.[22] However, this is numerically very inefficient since all pumped spin and charge currents in devices, where the precessing FM island is coupled to a region with SOC, are time-dependent.[19] Thus, one has to compute the scattering matrix of the device repeatedly at each time step of a discrete grid covering one period of harmonic external potential in order to find full ac current vs time dependence and then extract the *experimentally measured* dc component.

The relevant dc component of pumped current can be obtained from approaches which generalize the existing steady-state transport theories, such as the scattering matrix,[51,52] NEGF formalism,[38,40,41,53–56] and quantum master equations,[57] with the help of the Floquet theorem[58] valid for periodically driven systems. While the equations of the Floquet-NEGF formalism we adopt here have been used before to study a variety of charge pumping problems in noninteracting[40,53–55] and interacting electron systems[38,56] or photon-assisted dc transport,[41] the key issue is to find a solution to these equations that can capture pumping processes at arbitrary strength (or frequency) of the external time-periodic potential while *conserving*[50] charge currents at each step of analytic or numerical algorithm. For example, the often used continued fraction solution[40–43] to Floquet-NEGF equations does not[50] conserve charge current in the leads, and the key trick we employ below to ensure current conservation is the *reduced-zone scheme*.[38]

We begin the derivation for the charge-current-conserved Floquet-NEGF solution by noting that the two fundamental objects[59] of the NEGF formalism are the retarded

$$G^{r}_{\mathcal{I},\mathcal{J}}(t,t') \equiv -\frac{i}{\hbar}u(t-t')\langle\{\hat{d}_{\mathcal{I}}(t),\hat{d}^{\dagger}_{\mathcal{J}}(t')\}\rangle \quad (7)$$

and the lesser

$$G^{<}_{\mathcal{I},\mathcal{J}}(t,t') \equiv \frac{i}{\hbar}\langle\hat{d}^{\dagger}_{\mathcal{J}}(t')\hat{d}_{\mathcal{I}}(t)\rangle \quad (8)$$

Green functions which describe the density of available quantum states and how electrons occupy those states, respectively. Here u is the unit step function; indices $\{\mathcal{I},\mathcal{J}\} \in \{n,m,\mu,\nu,\sigma\}$ and creation $\hat{d}^{\dagger}$ or annihilation operators $\hat{d} \in \{\hat{a},\hat{b},\hat{c}\}$ are used. For notational convenience, the matrix representation with indices $\{\mathcal{I},\mathcal{J}\}$ will not be written out explicitly below.

The essence of the Floquet-NEGF approach is to treat the time variable t in Eq. (1) as an additional real-space degrees of freedom denoted by $\check{t}$ with considering the auxiliary

first-quantized Hamiltonian

$$\check{h}(\check{t}) = h(\check{t}) - i\hbar\frac{\partial}{\partial\check{t}}. \tag{9}$$

Here $h(\check{t})$ is the first-quantization version of our actual or original Hamiltonian (1); i.e., the matrix representation for $h(t)$ is of elements $h_{\mathcal{I}\mathcal{J}}(t)$ given by $H(t) = \sum_{\mathcal{I},\mathcal{J}} \hat{d}^\dagger_{\mathcal{I}}\hat{d}_{\mathcal{J}}h_{\mathcal{I}\mathcal{J}}(t)$. The check-hatted symbol $\check{X}$ is used to remind us that $\check{X}$ is an auxiliary variable or operator but not the actual one.

The Schrödinger equation for $\check{h}(\check{t})$ reads

$$i\hbar\frac{\partial}{\partial t}\check{\psi}(\check{t},t) = \check{h}(\check{t})\check{\psi}(\check{t},t), \tag{10}$$

while keeping in mind again that only t is the real time variable, but $\check{t}$ is a virtual position variable. It is straightforward to prove that, by assuming the wave function $\check{\psi}(\check{t},t)$ of the form $\check{\psi}(\check{t},t) = A(\check{t})B(t)$ in Eq.(10) and then letting $\check{t}\to t$, the original wave function is recovered,

$$\check{\psi}(\check{t}=t,t) = \psi(t), \tag{11}$$

where $\psi(t)$ obeys our original Schrödinger equation $i\hbar\partial\psi(t)/\partial t = h(t)\psi(t)$. Equation (11) plays the fundamental role in the Floquet NEGF, since it bridges the two systems, the auxiliary time-independent system described by $\check{h}(\check{t})$ and our original system described by $h(t)$. Accordingly, one can first solve the problems in the time-independent system constructed according to Eq. (9), express physical quantities or functions in terms of $\check{\psi}(\check{t},t)$, and eventually set $\check{t}\to t$ to obtain the corresponding physical quantities or functions for our original system.

To illustrate the idea above, consider the retarded Green function as an example. The retarded Floquet Green function $\check{G}^r(t,t';\check{t},\check{t}')$ corresponding to our auxiliary system $\check{h}(\check{t})$ obeys the equation of motion (EOM),

$$\left[i\hbar\frac{\partial}{\partial t} - \check{h}(\check{t})\right]\check{G}^r(t,t';\check{t},\check{t}') = \delta(t-t')\delta_T(\check{t}-\check{t}'), \tag{12}$$

where $\delta_T(\check{t}-\check{t}')$ denotes the Dirac delta function of period T. Note that $\check{h}(\check{t})$ is time independent; hence, $\check{G}^r(t,t';\check{t},\check{t}')$ depends only on the single time variable $t-t'$ via the Fourier transformation

$$\check{G}^r(t,t';\check{t},\check{t}') = \int_{-\infty}^{\infty}\frac{dE}{2\pi\hbar}e^{-iE(t-t')/\hbar}\check{G}^r(E;\check{t},\check{t}') \tag{13}$$

and can be expanded by the wave functions of the form

$$\check{G}^r(E;\check{t},\check{t}') = \sum_{n_{\rm ph},m_{\rm ph}=-\infty}^{\infty}\check{\psi}_{n_{\rm ph}}(\check{t}) \times\left[\frac{1}{(E+i\eta)I-\check{h}}\right]_{n_{\rm ph},m_{\rm ph}}\check{\psi}^*_{m_{\rm ph}}(\check{t}'). \tag{14}$$

Here, the notations, identity operator I, $\eta\to 0^+$, $\{n_{\rm ph},m_{\rm ph}\}\in$ integers, and $(\cdots)_{n_{\rm ph},m_{\rm ph}} \equiv \int_{-T/2}^{T/2}dt\check{\psi}^*_{n_{\rm ph}}(\check{t})(\cdots)\check{\psi}_{m_{\rm ph}}(\check{t})$ are used, and the basis

$$\check{\psi}_{n_{\rm ph}}(\check{t}) = (T)^{-1/2}e^{-in_{\rm ph}\omega\check{t}} \tag{15}$$

ensures the periodicity $\check{G}^r(E;\check{t}+lT,\check{t}'+l'T)$ with $\omega\equiv 2\pi/T$ and $\{l,l'\}\in$ integers. The $\{[(E+i\eta)I-\check{h}]^{-1}\}_{n_{\rm ph},m_{\rm ph}}$ in Eq. (14) is evaluated according to the definition (9) of $\check{h}$ via

$$\begin{aligned}\check{h}_{n_{\rm ph},m_{\rm ph}} &= \int_{-T/2}^{T/2}d\check{t}\check{\psi}^*_{n_{\rm ph}}(\check{t})\check{h}(\check{t})\check{\psi}_{m_{\rm ph}}(\check{t})\\ &= h_{n_{\rm ph},m_{\rm ph}} - n_{\rm ph}\hbar\omega\delta_{n_{\rm ph},m_{\rm ph}},\end{aligned} \tag{16}$$

with $n_{\rm ph}<0$ ($n_{\rm ph}>0$) accounting for the absorption (emission) processes of photons, as indicated by the subscript "ph", and

$$\begin{aligned}h_{n_{\rm ph},m_{\rm ph}} &= \int_{-T/2}^{T/2}d\check{t}\check{\psi}^*_{n_{\rm ph}}(\check{t})h(\check{t})\check{\psi}_{m_{\rm ph}}(\check{t})\\ &= \frac{1}{T}\int_{-T/2}^{T/2}d\check{t}e^{i(n_{\rm ph}-m_{\rm ph})\omega\check{t}}h(\check{t}).\end{aligned} \tag{17}$$

Note that here beside the $\{\mathcal{I},\mathcal{J}\}$ degrees of freedoms, the extra degree of freedom, namely the photon's, is introduced. The $h_{n_{\rm ph},m_{\rm ph}}$ exists in the $\{\mathcal{I},\mathcal{J}\}\otimes n_{\rm ph}$ Hilbert space, and thus so does $\check{G}^r(E;\check{t},\check{t}')$. The primary result for the actual (original) retarded Green function (7) is obtained by substituting (14), computed by Eqs. (15)–(17), into Eq. (13), and then replacing $\check{t}$ with t and $\check{t}'$ with t' in the wave-function-expanded Green function, namely, $\check{G}^r(t,t';\check{t},\check{t}')|_{\check{t}\to t,\check{t}'\to t'} = G^r(t,t')$; nonetheless $G^r(t,t')$ can be further simplified by noting the relation that for $l_{\rm ph}\in$ integers, one has

$$\begin{aligned}&\left[\frac{1}{(E+i\eta)I-\check{h}}\right]_{n_{\rm ph},m_{\rm ph}+l_{\rm ph}}\\ &\quad= \left[\frac{1}{(E+l_{\rm ph}\hbar\omega+i\eta)-\check{h}}\right]_{n_{\rm ph}-l_{\rm ph},m_{\rm ph}},\end{aligned} \tag{18}$$

which can be deduced simply from the observations that $\mathcal{M}\equiv(E+i\eta)I-\check{h}$ is a matrix of infinite size, and that $[(E+i\eta)I-\check{h}]_{n_{\rm ph},m_{\rm ph}+l_{\rm ph}}$ and $[(E+l_{\rm ph}\hbar\omega+i\eta)-\check{h}]_{n_{\rm ph}-l_{\rm ph},m_{\rm ph}}$ evaluated according to Eqs. (16) and (17) are at the same position of $\mathcal{M}$, i.e., the same matrix element of $\mathcal{M}$; therefore, the element at the same matrix position of $\mathcal{M}^{-1}$ implies Eq. (18), a manifestation of the reduced-zone scheme in which the energy E can be reduced to the zone of range $\hbar\omega$. With the help of $\{[(E+i\eta)I-\check{h}]^{-1}\}_{n_{\rm ph},m_{\rm ph}} = \{[(E+m_{\rm ph}\hbar\omega+i\eta)-\check{h}]^{-1}\}_{n_{\rm ph}-m_{\rm ph},0}$ [$m_{\rm ph}=0$ and the renotation $l_{\rm ph}\to m_{\rm ph}$ in Eq. (18)] and change of variables, $E'\equiv E+m_{\rm ph}\hbar\omega$ and $n'_{\rm ph}\equiv n_{\rm ph}-m_{\rm ph}$, the retarded Green function now reads

$$\begin{aligned}G^r(t,t') &= \check{G}^r(t,t';\check{t},\check{t}')|_{\check{t}\to t,\check{t}'\to t'}\\ &= \frac{1}{T}\int_{-\infty}^{\infty}\frac{dE}{2\pi\hbar}e^{-iE(t-t')/\hbar}\sum_{n_{\rm ph},m_{\rm ph}=-\infty}^{\infty}e^{-in_{\rm ph}\omega t}e^{im_{\rm ph}\omega t'}\\ &\quad\times\left[\frac{1}{(E+i\eta)I-\check{h}}\right]_{n_{\rm ph},m_{\rm ph}}\\ &= \delta(0)\int_{-\infty}^{\infty}\frac{dE'}{2\pi\hbar}e^{-iE'(t-t')/\hbar}\\ &\quad\times\sum_{n'_{\rm ph}=-\infty}^{\infty}e^{-in'_{\rm ph}\omega t}\check{G}^r_{n'_{\rm ph},0}(E'),\end{aligned} \tag{19}$$

with $\check{G}^r_{n_{\rm ph},m_{\rm ph}}(E)\equiv\{[(E+i\eta)I-\check{h}]^{-1}\}_{n_{\rm ph},m_{\rm ph}} = \check{G}^r_{n_{\rm ph}-m_{\rm ph},0}(E+m_{\rm ph}\hbar\omega)$; note that the prefactor $\delta(0)$ in Eq. (19) is due

to the cancelation of $m_{\rm ph}\hbar\omega$ in the exponent, i.e., $\delta(0) = (T)^{-1}\sum_{m_{\rm ph}} 1 = (T)^{-1}\sum_{m_{\rm ph}} e^{-im_{\rm ph}\hbar\omega\times 0}$, while for physical quantities, this prefactor $\delta(0)$ is irrelevant; instead, it is the normalized [absence of $\delta(0)$ in Eq. (19)] Green function,

$$\bar{G}^r(t,t') \equiv \int_{-\infty}^{\infty}\frac{dE}{2\pi\hbar}e^{-iE(t-t')/\hbar}\sum_{n_{\rm ph}=-\infty}^{\infty}e^{-in_{\rm ph}\omega t}\check{G}^r_{n_{\rm ph},0}(E), \tag{20}$$

that renders physical observables. One can also verify that the expression (20) satisfies the EOM,

$$\left[i\hbar\frac{\partial}{\partial t}-h(t)\right]\bar{G}^r(t,t') = \delta_T(t-t'), \tag{21}$$

by applying $\int_{-T/2}^{T/2}dt'$ to both sides of the above Eq. (21). Comparing the EOMs (12) and (21), one clearly sees that the evolution of $\bar{G}^r(t,t')$ is governed by the actual system $h(t)$, while $\check{G}^r(t,t';\check{t},\check{t}')$ is by the auxiliary system $\check{h}(\check{t})$.

The lesser Green function can be obtained in the same manner. The auxiliary lesser Green function obeys the Keldysh integral equation,

$$\begin{aligned}\check{G}^<(t,t';\check{t},\check{t}') &= \int_{-\infty}^{\infty}\int_{-\infty}^{\infty}dt_1dt_2\int_{-T/2}^{T/2}\int_{-T/2}^{T/2}d\check{t}_1d\check{t}_2\check{G}^r(t,t_1;\check{t},\check{t}_1)\\ &\times\check{\Sigma}^<(t_1,t_2;\check{t}_1,\check{t}_2)\check{G}^a(t_2,t';\check{t}_2,\check{t}').\end{aligned} \tag{22}$$

The time-independent $\check{h}(\check{t})$ allows $\check{G}^<(t,t';\check{t},\check{t}')$ to be expressed in terms of the single time variable $t-t'$ of the form

$$\begin{aligned}&\check{G}^<(t,t';\check{t},\check{t}')\\ &= \int_{-\infty}^{\infty}\frac{dE}{2\pi\hbar}e^{-iE(t-t')/\hbar}\check{G}^<(E;\check{t},\check{t}'),\end{aligned} \tag{23}$$

with $\check{G}^<(E;\check{t},\check{t}')$ being Eq. (22) written in the energy domain,

$$\begin{aligned}\check{G}^<(E;\check{t},\check{t}') &= \int_{-T/2}^{T/2}\int_{-T/2}^{T/2}d\check{t}_1d\check{t}_2\check{G}^r(E;\check{t},\check{t}_1)\check{\Sigma}^<(E;\check{t}_1,\check{t}_2)\\ &\times\check{G}^a(E;\check{t}_2,\check{t}').\end{aligned} \tag{24}$$

Here $\check{G}^a(E;\check{t},\check{t}') = [\check{G}^r(E;\check{t}',\check{t})]^\dagger$ is the advanced Green function, and $\check{\Sigma}^<(E;\check{t},\check{t}') = |\gamma_0|^2\check{g}^<(E;\check{t},\check{t}') = \sum_p|\gamma_0|^2\check{g}^{(p)<}(E;\check{t},\check{t}')$ is the lesser self-energy accounting for the interactions from all probes with the bare (probes that are free of interacting with the environments) lesser Green function of probe p denoted by $\check{g}^{(p)<}(E;\check{t},\check{t}')$. The primary result for the lesser Green function (8) is obtained via $\check{G}^<(t,t';\check{t},\check{t}')|_{\check{t}\to t,\check{t}'\to t'} = G^<(t,t')$ where $\check{G}^<(t,t';\check{t},\check{t}')$ is computed by the Green functions in the *time-independent* system $\check{h}(\check{t})$ according to Eqs. (23) and (24). Similarly, $G^<(t,t')$ can also be further simplified by taking advantage of relation (18) and change of variables. For this simplification, we utilize the Keldysh equation in the energy domain Eq. (24) and the wave-function expansion to obtain the expression of $\check{G}^<(t,t';\check{t},\check{t}')$,

$$\begin{aligned}\check{G}^<(t,t';\check{t},\check{t}') &= \frac{1}{T}\int_{-\infty}^{\infty}\frac{dE}{2\pi\hbar}e^{-iE(t-t')/\hbar}\sum_{n_{\rm ph},m_{\rm ph}=-\infty}^{\infty}\sum_{k_{\rm ph},l_{\rm ph}=-\infty}^{\infty}e^{-in_{\rm ph}\omega\check{t}}\left[\frac{1}{(E+i\eta)I-\check{h}}\right]_{n_{\rm ph},k_{\rm ph}}\\ &\times\sum_p|\gamma_0|^2\check{g}^{(p)<}_{k_{\rm ph},l_{\rm ph}}(E)\left[\frac{1}{(E-i\eta)I-\check{h}^\dagger}\right]_{l_{\rm ph},m_{\rm ph}}e^{im_{\rm ph}\omega\check{t}'}\\ &= \frac{1}{T}\int_{-\infty}^{\infty}\frac{dE'}{2\pi\hbar}e^{-i(E'-m_{\rm ph}\hbar\omega)(t-t')/\hbar}\sum_{n_{\rm ph},m_{\rm ph}=-\infty}^{\infty}e^{-in_{\rm ph}\omega\check{t}}e^{im_{\rm ph}\omega\check{t}'}\sum_{k_{\rm ph},l'_{\rm ph}=-\infty}^{\infty}\left[\frac{1}{(E'-m_{\rm ph}\hbar\omega+i\eta)I-\check{h}}\right]_{n_{\rm ph},k_{\rm ph}}\\ &\times\sum_p|\gamma_0|^2\check{g}^{(p)<}_{k_{\rm ph},l'_{\rm ph}+m_{\rm ph}}(E'-m_{\rm ph}\hbar\omega)\left[\frac{1}{(E'-i\eta)I-\check{h}^\dagger}\right]_{l'_{\rm ph},0},\end{aligned} \tag{25}$$

where $\{[(E-i\eta)I-\check{h}^\dagger]^{-1}\}_{l_{\rm ph},m_{\rm ph}} = \{[(E+m_{\rm ph}\hbar\omega-i\eta)I-\check{h}^\dagger]^{-1}\}_{l_{\rm ph}-m_{\rm ph},0}$ and change of variables $E'\equiv E+m_{\rm ph}\hbar\omega$ and $l'_{\rm ph}\equiv l_{\rm ph}-m_{\rm ph}$ are used. Note that the *original* Hamiltonian (5) of the NM probes in our present case is time independent so that we have the expression $|\gamma_0|^2\check{g}^{(p)<}_{n_{\rm ph},m_{\rm ph}}(E) = -2i\check{f}^{(p)}_{n_{\rm ph}}(E)|\gamma_0|^2{\rm Im}\check{g}^{(p)r}_{n_{\rm ph},m_{\rm ph}}(E) = i\check{f}^{(p)}_{n_{\rm ph}}(E)\check{\Gamma}^{(p)}_{n_{\rm ph},m_{\rm ph}}(E)$, with the Fermi-Dirac distribution (of Fermi energy E_F at zero temperature as the regime we are interested in)

$$\begin{aligned}\check{f}^{(p)}_{n_{\rm ph}}(E) &= \check{f}^{(p)}(E+n_{\rm ph}\hbar\omega)\\ &= \lim_{\beta\to0}[1+e^{(E+n_{\rm ph}\hbar\omega-E_F)/\beta}]^{-1}\end{aligned} \tag{26}$$

and

$$\begin{aligned}\check{\Gamma}^{(p)}_{n_{\rm ph},m_{\rm ph}}(E) &= i|\gamma_0|^2\{[(E+i\eta)I-\check{h}^{(p)}]^{-1}\\ &-[(E-i\eta)I-\check{h}^{(p)\dagger}]^{-1}\}_{n_{\rm ph},m_{\rm ph}}.\end{aligned} \tag{27}$$

Here the definition (9) yields $\check{h}^{(p)}(\check{t}) = h^{(p)}-i\hbar\partial/\partial\check{t}$ with $h^{(p)}$ being the first-quantized version of $H_{\rm NM} = \sum_p h^{(p)}\hat{b}_p^\dagger\hat{b}_p$, and note again because $H_{\rm NM}$ in Eq. (5) or $h^{(p)}$ is time independent, one has $[h^{(p)}]_{n_{\rm ph},m_{\rm ph}} = \delta_{n_{\rm ph},m_{\rm ph}}[h^{(p)}]_{n_{\rm ph}}$, resulting in $\check{\Gamma}^{(p)}_{n_{\rm ph},m_{\rm ph}}(E)$ proportional to $\delta_{n_{\rm ph},m_{\rm ph}}$, i.e., diagonal, and thus the bare lesser Green functions of NMs are diagonal in photon (or Floquet) space $\check{g}^{(p)<}_{n_{\rm ph},m_{\rm ph}}(E) = \delta_{n_{\rm ph},m_{\rm ph}}\check{g}^{(p)<}_{n_{\rm ph}}(E)$ as well. Moreover, applying the same argument we used to derive Eq. (18) to $\check{g}^{(p)<}_{n_{\rm ph},m_{\rm ph}}(E)$ evaluated by Eqs. (26) and (27), one deduces

$$\check{g}^{(p)<}_{n_{\rm ph},m_{\rm ph}+l_{\rm ph}}(E) = \check{g}^{(p)<}_{n_{\rm ph}-l_{\rm ph},m_{\rm ph}}(E+l_{\rm ph}), \tag{28}$$

which reflects again the reducible property (energy E can be reduced to the zone of range $\hbar\omega$) that yields the reduced-zone scheme. Using above relation (28) and change of variables

$k'_{\rm ph} \equiv k_{\rm ph} - m_{\rm ph}$ and $n'_{\rm ph} \equiv n_{\rm ph} - m_{\rm ph}$ in Eq. (25), we arrive at

$$\begin{aligned}\check{G}^<(t,t';\check{t},\check{t}') &= \frac{1}{T}\int_{-\infty}^{\infty}\frac{dE'}{2\pi\hbar}e^{-i(E'-m_{\rm ph}\hbar\omega)(t-t')/\hbar}\sum_{n'_{\rm ph},m_{\rm ph}}e^{-i(n'_{\rm ph}+m_{\rm ph})\omega\check{t}}e^{im_{\rm ph}\omega\check{t}'}\\ &\times\sum_{k'_{\rm ph},l'_{\rm ph}}\left[\frac{1}{(E'+i\eta)I-\check{h}}\right]_{n'_{\rm ph},k'_{\rm ph}}\\ &\times\sum_p|\gamma_0|^2\check{g}^{(p)<}_{k'_{\rm ph},l'_{\rm ph}}(E')\left[\frac{1}{(E'-i\eta)I-\check{h}^\dagger}\right]_{l'_{\rm ph},0}. \qquad (29)\end{aligned}$$

The actual lesser Green function can be obtained again via setting $\check{t}\to t$ and $\check{t}'\to t'$ in Eq. (29) and noting that $m_{\rm ph}\hbar\omega$ in the exponent is canceled out; we thus have $\delta(0) = (T)^{-1}\sum_{m_{\rm ph}} 1 = (T)^{-1}\sum_{m_{\rm ph}} e^{-im_{\rm ph}\hbar\omega\times 0}$, so that the actual lesser Green function can be written as

$$\begin{aligned}G^<(t,t') &= \check{G}^<(t,t';\check{t},\check{t}')|_{\check{t}\to t,\check{t}'\to t'}\\ &= \delta(0)\int_{-\infty}^{\infty}\frac{dE'}{2\pi\hbar}e^{-iE'(t-t')/\hbar}\sum_{n'_{\rm ph}}e^{-in'_{\rm ph}\omega t}\\ &\times\sum_{k'_{\rm ph},l'_{\rm ph}}\left[\frac{1}{(E'+i\eta)I-\check{h}}\right]_{n'_{\rm ph},k'_{\rm ph}}\\ &\times\sum_p\check{g}^{(p)<}_{k'_{\rm ph},l'_{\rm ph}}(E')\left[\frac{1}{(E'-i\eta)I-\check{h}^\dagger}\right]_{l'_{\rm ph},0},\end{aligned}$$

and eventually obtain the normalized lesser Green function,

$$\begin{aligned}\bar{G}^<(t,t') &= \int_{-\infty}^{\infty}\frac{dE}{2\pi\hbar}e^{-iE(t-t')/\hbar}\sum_{n_{\rm ph}}e^{-in_{\rm ph}\omega t}\\ &\times\sum_{k_{\rm ph},l_{\rm ph}}\left[\frac{1}{(E+i\eta)I-\check{h}}\right]_{n_{\rm ph},k_{\rm ph}}\\ &\times\sum_p|\gamma_0|^2\check{g}^{(p)<}_{k_{\rm ph},l_{\rm ph}}(E)\left[\frac{1}{(E-i\eta)I-\check{h}^\dagger}\right]_{l_{\rm ph},0}. \qquad (30)\end{aligned}$$

Physical quantities can be extracted from the actual Green function (30). For instance, the quantum-statistical-averaged occupation number at time t on site $i\in\{n,m,\mu\}$ can be expressed as $\mathrm{Tr}_{\rm s}[\bar{G}^<_{i,i}(t,t)O]\hbar/i$, while the bond current from site i to site j reads

$$J_{i\to j}(t) = -\mathrm{Tr}_{\rm s}\left[\frac{\{h_{j,i},O\}}{2}\bar{G}^<_{i,j}(t,t) - \frac{\{h_{i,j},O\}}{2}\bar{G}^<_{j,i}(t,t)\right], \qquad (31)$$

with $O = I_s$ ($O = S_q$) for particle (spin S_q) occupations or currents and I_s being the 2×2 identity matrix in the Pauli space; the notation $\mathrm{Tr}_{\rm s}$ stands for performing the trace in the Pauli space (spin Hilbert space), and the anticommutator $\{A,B\}$ is defined as $AB + BA$. The particle (charge) current

$$\begin{aligned}I_p(t) &= \frac{1}{2\pi\hbar}\sum_{p'}\sum_{n_{\rm ph},m_{\rm ph}}\int_{E_F-\hbar\omega/2}^{E_F+\hbar\omega/2}dE\\ &\times\mathrm{Tr}'[\check{G}^r(E)\check{f}^{(p')}(E)\check{\Gamma}^{(p')}(E)\check{G}^a(E)\check{\Gamma}^{(p)}(E)\\ &-\check{G}^r(E)\check{\Gamma}^{(p')}(E)\check{G}^a(E)\check{f}^{(p)}(E)\check{\Gamma}^{(p)}(E)]_{n_{\rm ph},m_{\rm ph}}\\ &\times e^{-i(n_{\rm ph}-m_{\rm ph})\omega t} \qquad (32)\end{aligned}$$

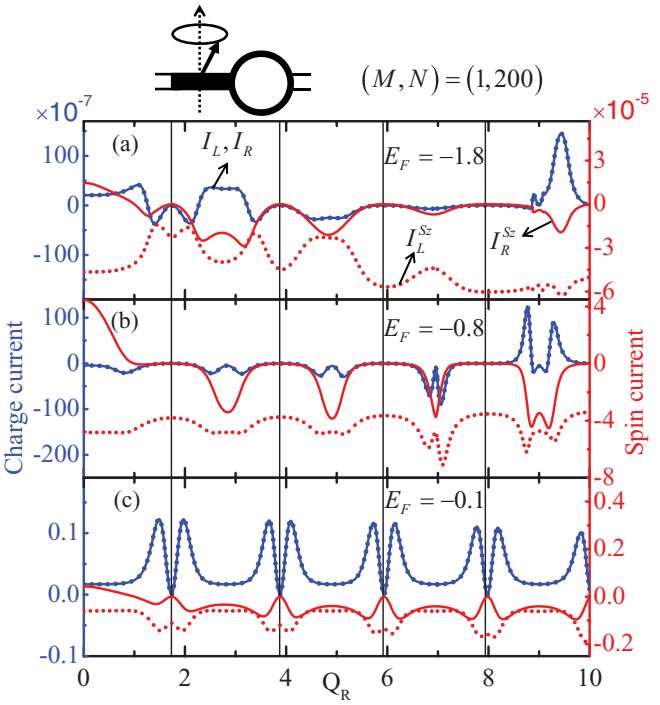

FIG. 2. (Color online) Pumped charge and spin currents as a function of the dimensionless Rashba spin-orbit coupling strength Q_R in the two-terminal spin-driven setup (top schematics) with ring size $(M,N) = (1,200)$ at different Fermi energies (a) $E_F = -1.8$, (b) $E_F = -0.8$, and (c) $E_F = -0.1$. The ring is in contact with two semi-infinite one-dimensional leads in which currents are probed. The solid vertical lines here indicate the current modulation nodes Q^*_R at which the complete destructive interferences for spin-z take place, causing $I_R = I^{S_z}_R = 0$. Since charge currents are conserved, $I_L = I_R$ is satisfied. The spin-driven results here correspond to the electric-driven results, Fig. 3 in Ref. 34.

and spin current

$$\begin{aligned}I^{S_q}_p(t) &= \frac{1}{4\pi}\sum_{p'}\sum_{n_{\rm ph},m_{\rm ph}}\int_{E_F-\hbar\omega/2}^{E_F+\hbar\omega/2}dE\\ &\times\mathrm{Tr}'[\sigma_q\check{G}^r(E)\check{f}^{(p')}(E)\check{\Gamma}^{(p')}(E)\check{G}^a(E)\check{\Gamma}^{(p)}(E)\\ &-\check{G}^r(E)\check{\Gamma}^{(p')}(E)\check{G}^a(E)\check{f}^{(p)}(E)\check{\Gamma}^{(p)}(E)]_{n_{\rm ph},m_{\rm ph}}\\ &\times e^{-i(n_{\rm ph}-m_{\rm ph})\omega t} \qquad (33)\end{aligned}$$

probed by lead p are obtained by summing all the bond currents (31) flowing through lead p. Note here the notation Tr' performs the trace over all degrees of freedom, *except* the photon's. All the functions within the trace are matrices; for example, the Fermi-Dirac distribution is a matrix, $\check{f}^{(p)}(E) = \check{f}^{(p)}_{n_{\rm ph}}(E)\delta_{n_{\rm ph},m_{\rm ph}}$, computed by Eq. (26). The time-averaged currents can then be obtained via $I_p \equiv \mathrm{sign}(p)\times 2\pi\hbar T^{-1}\int_{-T/2}^{T/2}dt\, I_p(t)$ and $I^{S_q}_p \equiv \mathrm{sign}(p)\times 4\pi T^{-1}\int_{-T/2}^{T/2}dt\, I^{S_q}_p(t)$ as

$$\begin{aligned}I_p &= \mathrm{sign}(p)\sum_{p'}\int_{E_F-\hbar\omega/2}^{E_F+\hbar\omega/2}dE\,\mathrm{Tr}[\check{G}^r(E)\check{f}^{(p')}(E)\check{\Gamma}^{(p')}(E)\\ &\times\check{G}^a(E)\check{\Gamma}^{(p)}(E)\\ &-\check{G}^r(E)\check{\Gamma}^{(p')}(E)\check{G}^a(E)\check{f}^{(p)}(E)\check{\Gamma}^{(p)}(E)] \qquad (34)\end{aligned}$$

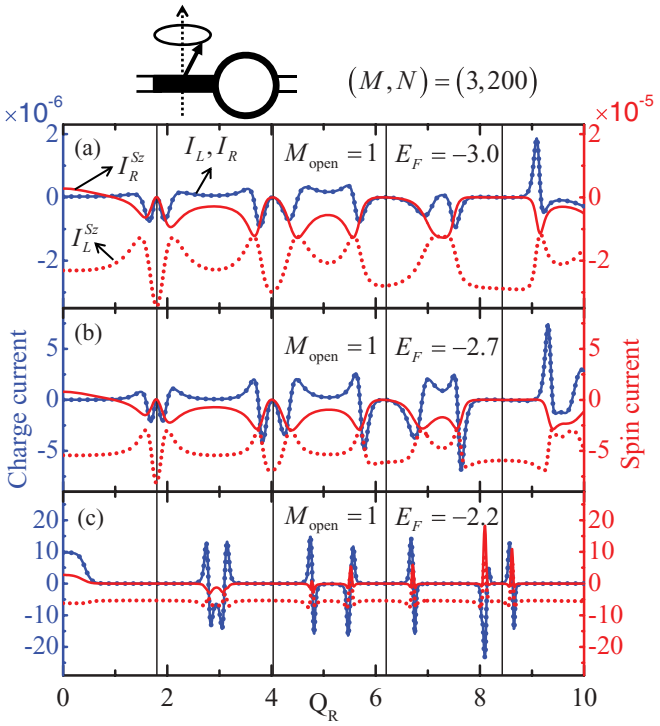

FIG. 3. (Color online) Pumped charge and spin currents as a function of the dimensionless Rashba spin-orbit coupling strength Q_R in the two-terminal spin-driven setup (top schematics) at different Fermi energies (a) $E_F = -3.0$, (b) $E_F = -2.7$, and (c) $E_F = -2.2$ that yield the number of open channels, $M_{\rm open} = 1$. The ring is of size $(M,N) = (3,200)$ and in contact with two semi-infinite probes of width consisting of three lattice sites. The solid vertical lines here indicate the current modulation nodes Q_R^*. The spin-driven results here correspond to the electric-driven results, Fig. 5 in Ref. 34.

and

$$I_p^{S_q} = \mathrm{sign}(p)\sum_{p'}\int_{E_F-\hbar\omega/2}^{E_F+\hbar\omega/2} dE \times \mathrm{Tr}\{\sigma_q[\check{G}^r(E)\check{f}^{(p')}(E)\check{\Gamma}^{(p')}(E)\check{G}^a(E)\check{\Gamma}^{(p)}(E) - \check{G}^r(E)\check{\Gamma}^{(p')}(E)\check{G}^a(E)\check{f}^{(p)}(E)\check{\Gamma}^{(p)}(E)]\}, \quad (35)$$

with $\mathrm{sign}(p) = 1$ for $p \in \{R,T\}$ and $\mathrm{sign}(p) = -1$ for $p \in \{L,B\}$. Notice here the appearance of $\mathrm{sign}(p)$ is merely for the sign convenience, positive for right- or up-flowing currents, while negative for left- or down-flowing currents. The prefactor $2\pi\hbar$ (4π) for I_p ($I_p^{S_q}$) is adopted so that the units of I_p and $I_p^{S_q}$ are the same. In other words, if I_p measures the number of charge quanta flowing through the lead p per second, then $I_p^{S_q}$ measures the number of spin S_q quanta flowing through the lead p per second. The trace here now is taken over all degrees of freedom, including the photon's.

We emphasize that in Eqs. (32)–(35), the reduced-zone scheme[38] such as (18) or (28) is adopted, so that the original integral interval $[-\infty,\infty]$ over energy E is reduced to $[E_F - \hbar\omega/2, E_F + \hbar\omega/2]$, and with this scheme, for any given maximum $n_{\rm ph}^{\rm max} \geqslant |n_{\rm ph}|$, charge currents are conserved, namely, $\sum_p I_p(t) = 0$ or $\sum_p \mathrm{sign}(p) I_p = 0$ (see Appendix for more details). In principle all integers $n_{\rm ph}$ should account for transport; i.e., transitions involving any number of photons have to be taken into account. Nonetheless when the strength of the time-dependent field is small, only a few photons can be absorbed or emitted by electrons near the Fermi level, and thus considering transitions between channels of a few photons is sufficient to get accurate results of currents. In our following calculations, $|n_{\rm ph}| \leqslant 2$ is chosen, since we find $|n_{\rm ph}| \leqslant 2$ and $|n_{\rm ph}| \leqslant 3$ do not yield significantly discernible results.

IV. RESULTS AND DISCUSSION

By Eqs. (34) and (35), we show and examine our numerical results for two- and four-terminal spin-pumping setups with

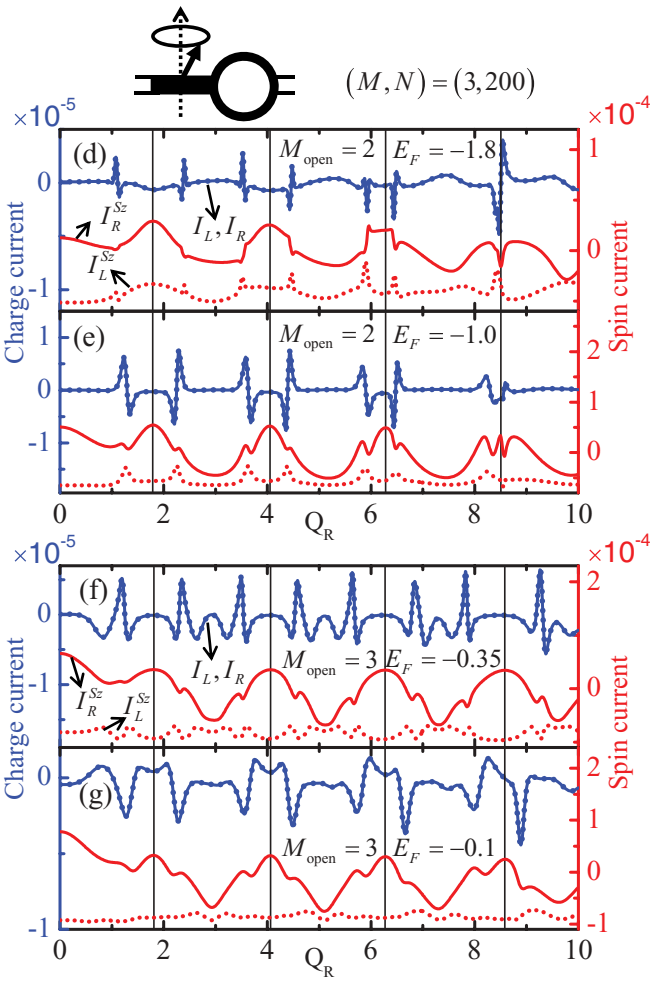

FIG. 4. (Color online) Pumped charge and spin currents as a function of the dimensionless Rashba spin-orbit coupling strength Q_R in the spin-driven setup the same as considered in Fig. 3, while different Fermi energies are chosen to have the number of open channels, $M_{\rm open} = 2$ for (d) $E_F = -1.8$ and (e) $E_F = -1.0$ and $M_{\rm open} = 3$ for (f) $E_F = -0.35$ and (g) $E_F = -0.1$. Unlike (a), (b), and (c) with $M_{\rm open} = 1$ in Fig. 2, the modulation here becomes incomplete (absence of the AC-spin-interference-induced modulation nodes at which one has $I_R = I_R^{S_z} = 0$, namely, absence of Q_R^*s) due to the loss of $M_{\rm open} = 1$, while the (incomplete) quasiperiodicity can still be found as depicted by the solid vertical lines. The spin-driven results here correspond to the electric-driven results, Fig. 6 in Ref. 34.

the parameters and units specified in Sec. IV A. In Sec. IV B, we first concentrate on the two-terminal case [Fig. 1(b)] to see the counterpart physics shown in Ref. 34 and then, in Sec. IV C, we investigate the four-terminal case [Fig. 1(a)] to unveil the phenomena dual to what were found in Ref. 35. Our discussions are restricted to the case of single precessing FM in Secs. IV B and IV C. In Sec. IV D, we aim at building up the relations between probed currents in the same or different pumping configurations from the symmetry perspective; the two presented symmetries yield the invariant AC ring Hamiltonian, and the arguments on the relations based on the symmetries are generally capable of setups of an arbitrary number of precessing FM islands and terminals. Nevertheless, for demonstration simplicity, below in Sec. IV E, where our numerical results are shown to be in line with the predictions given by the symmetry arguments, we consider only the two-terminal two-precessing-FM setups.

A. Parameters and units

The following parameters and units are used. All energies are in units of the hopping energy γ_0, and lengths are in units of the lattice constant a. For brevity, the aspect ratio $1/2$ between the length of FM, $L_{\rm FM}$, and the length of the AC ring, N, is adopted; for example, in Fig. 1(b), we have $L_{\rm FM}/N = 4/8$. Also, the width of FM is set to be the same as the width of

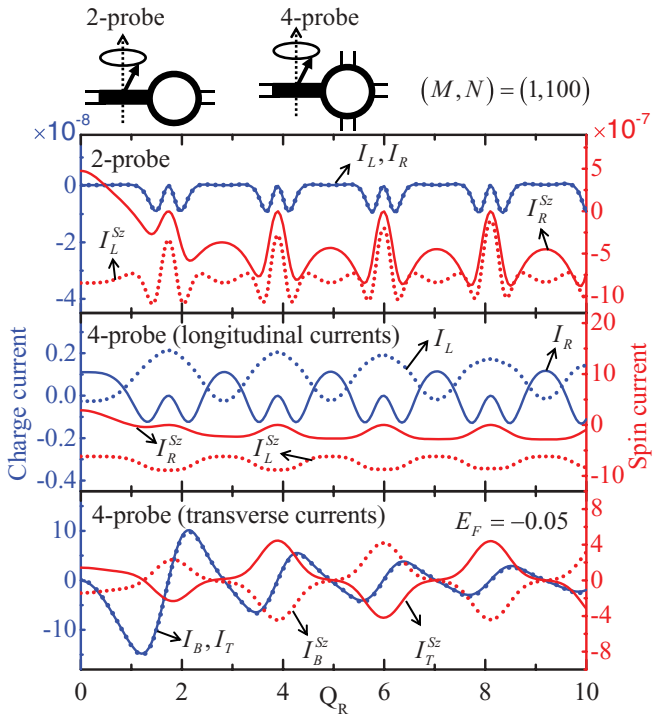

FIG. 5. (Color online) Pumped charge and spin currents as a function of the dimensionless Rashba spin-orbit coupling strength Q_R in the two-terminal (top panel) and four-terminal (middle and bottom panels) spin-driven setups (see the schematics) in which the same strict one-dimensional ring of size $(M,N)=(1,100)$ is considered. Each of the probes is one-dimensional. The complete modulation nodes Q_R^* that characterize the quasiperiodicity emerge through $I_R = I_R^{S_z} = 0$ in both two- and four-terminal setups. In the four-terminal setup, the transverse currents with $I_B = I_T$ and $I_B^{S_z} + I_T^{S_z} = 0$ for all Q_R reflect the existence of the inverse spin-Hall effect, and the quasiperiodicity can also be identified via $I_B = I_T = 0$ at the same Q_R^*s. Note that the Onsager relation is preserved if we compare with the finding in the electric-driven setup, Fig. 2 in Ref. 35.

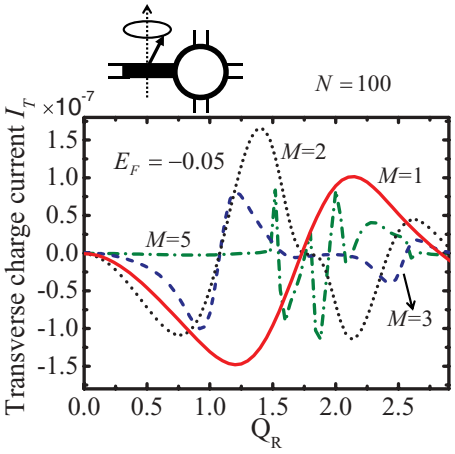

FIG. 6. (Color online) Pumped transverse charge currents $I_T = I_B$ at different ring width M as a function of the dimensionless Rashba spin-orbit coupling strength Q_R in the four-terminal spin-driven setup (top schematics) with four semi-infinite one-dimensional probes. Refer to Fig. 3 in Ref. 35 for the reciprocal Onsager (electric-driven) results.

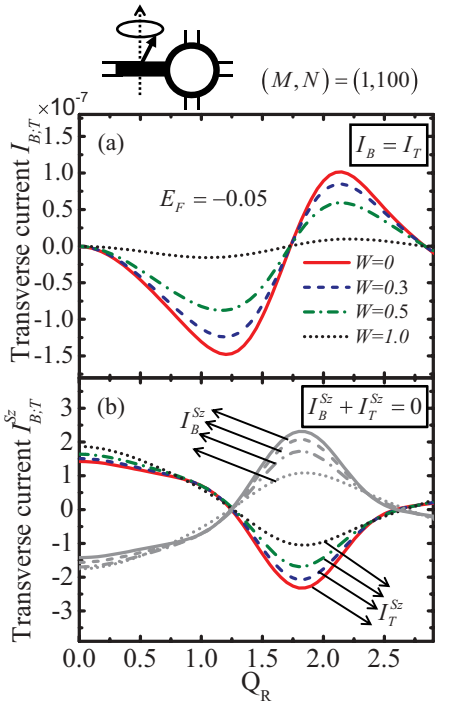

FIG. 7. (Color online) Pumped transverse (a) charge and (b) spin-z currents versus the dimensionless Rashba spin-orbit coupling strength Q_R. The inverse spin-Hall effect (shown through $I_B = I_T$ and $I_B^{S_z} + I_T^{S_z} = 0$) survives in the weak-disorder regime with different disorder strengths W of the ring in the four-terminal (each of the probes is one-dimensional) spin-driven setup (top schematics). The reciprocal Onsager (electric-driven) result is shown in Fig. 4 of Ref. 35.

NM. The default values of parameters of the precession FM (FMs), the spin splitting strength $\Delta = 1$, precession frequency (energy) $\hbar\omega = 10^{-3}$, precession cone angle $\Theta = 10^{\circ}$, and initial precession phase (azimuthal angle) $\Phi = 0^{\circ}$, are chosen. To compare the results of our spin-driven setups with the findings of the electric-driven setups in Refs. 34 and 35, the size of the AC ring are set similar or according to Refs. 34 and 35. We refer to the ring of $M = 1$ as the strict 1D ring, and $M > 1$ as the quasi-1D ring. Note again that the sign convention used here is positive for right- or up-moving flow and negative for left- or down-moving flow. No bias is applied to any probes for what we consider here are all spin-driven setups. The number of open channels M_{open} in the leads is adjustable by varying E_F; referring to Fig. 2 in Ref. 34, for leads of width consisting of three lattice sites, one has $M_{\text{open}} = 1$ approximately in the interval $E_F \in [\pm 3.9, \pm 2]$, $M_{\text{open}} = 2$ in $E_F \in [\pm 2, \pm 0.5]$, and $M_{\text{open}} = 3$ in $E_F \in [-0.5, 0.5]$.

B. Single precessing FM island attached to two-terminal mesoscopic AC ring

We begin with the two-terminal case of the clean AC ring in the spin-driven setup Fig. 1(b). Introducing the dimensionless Rashba SOC strength,

$$Q_R \equiv \frac{\gamma_{\text{SO}} N}{\gamma_0 \pi}, \tag{36}$$

the special case of the strict 1D ring yields the conductance of the form[27] $e^2/h\{1 + \cos[\pi(\sqrt{Q_R^2 + 1} - 1)]\}$ which gives the complete destructive interference condition, $Q_R^* = \sqrt{l^2 - 1}$ ($l = 2, 4, 6, \ldots$). Although this expression ignores the scattering at the interface between the ring and the leads, our numerical calculations, which take into account all interfacial scattering, suggests that these Q_R^*s are still preserved even in the presence of the above scattering. As shown in Fig. 2 for $(M, N) = (1, 200)$, the pumped spin-z current $I_R^{S_z} = 0$ vanishes at these Q_R^*s, where the charge current $I_R = I_L = 0$ also disappears, consistent with the electric-driven results.[27,33,34] Similar behavior can be found for the quasi-1D ring with only one channel open ($M_{\text{open}} = 1$). As shown in Fig. 3 with $(M, N) = (3, 200)$, the Q_R^* (AC-spin-interference-induced) modulation nodes still exist, but are altered. We will address the reason of this alternation later. For now we focus first on the origination and the clarification of the Q_R^*s.

The $I_R^{S_z}$ modulation originates from the fact that a spin-z acquires some AC phase induced by the Rashba SOC when

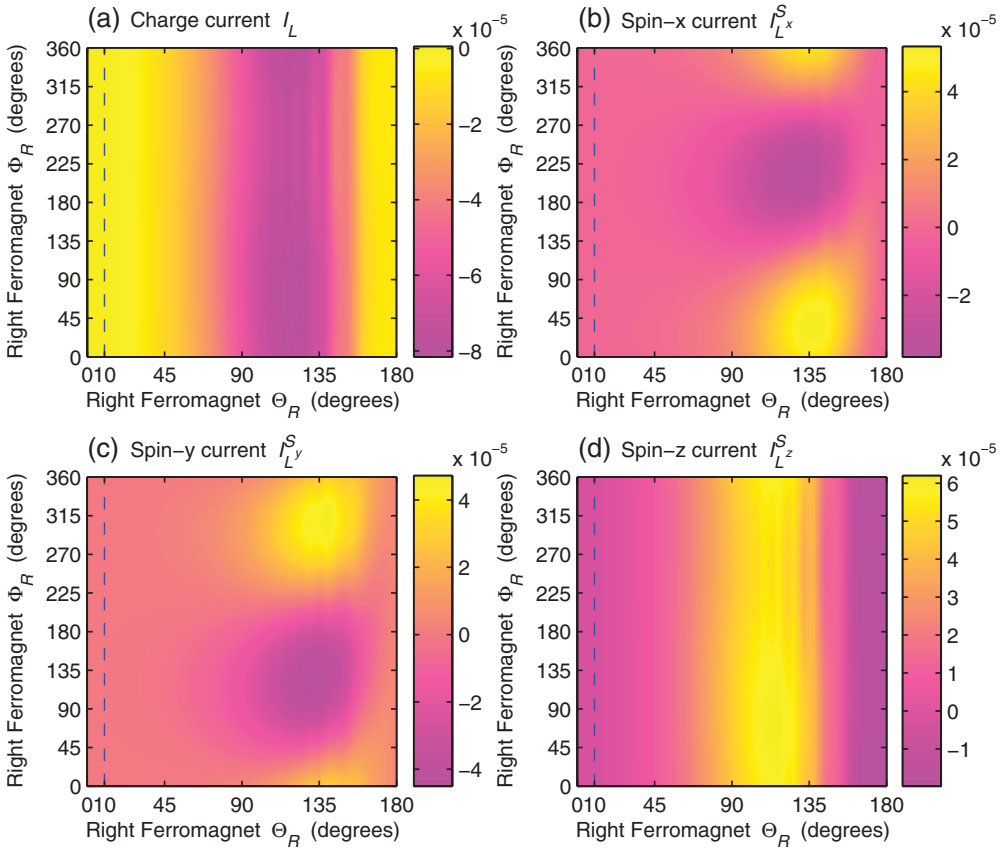

FIG. 8. (Color online) Pumped (a) charge current and (b) spin-x, (c) spin-y, and (d) spin-z currents, in the two-terminal two-precessing-ferromagnet ring device as shown in the schematics of Fig. 10, probed by the left lead as functions of precession cone angle Θ_R and initial precession phase (azimuthal angle) Φ_R of the right ferromagnet. The ring is of size $(M, N) = (1, 200)$ and of the dimensionless Rashba spin-orbit coupling strength $Q_R = 5$. The left ferromagnet is of $\Theta_L = 10^{\circ}$ (represented by the dashed lines) and $\Phi_L = 0^{\circ}$. The left and right leads are one-dimensional, i.e., the number of open channel $M_{\text{open}} = 1$ with Fermi energy $E_F = -1.8$.

passing through the AC ring, and the phase difference between the upper arm and lower arm of the ring depends on the Rashba SOC strength; accordingly, gradually varying the Rashba SOC strength modulates the spin-z current. The condition of only one open channel $M_{\text{open}} = 1$ is satisfied when $M = 1$ (Fig. 2), or when $M > 1$ (Fig. 3) with the Fermi energy E_F only crossing one subband of the leads. In the former (strict 1D), Q_R^*s are independent of the Fermi energy E_F, while in the latter (quasi 1D), when one tunes E_F but keeps E_F in the regime $M_{\text{open}} = 1$, Q_R^*s also remain unaffected (independent of E_F as long as $M_{\text{open}} = 1$ is satisfied), mimicking again the electric-driven setup. Moreover, since the spin-z current I^{S_z} pumped by the FM is pure, if the spin-z encounters a complete destructive interference, i.e., not able to transport through the ring, then no charge currents will be generated in the right NM as well, providing that no passage of spins with different polarizations such as spin-x or spin-y occur through the interface between the right NM and AC ring as we will address below. We refer to these types of nodes as the *AC-spin-interference-induced* modulation nodes where $I_R^{S_z} = 0$ and I_R vanish concurrently at the same Q_R^*s, as indicated by the solid vertical lines in Figs. 2 and 3.

Note that when a pumped spin-z enters the ring, it starts to precess, and there are chances for this spin to become spin-x or spin-y when leaving the ring to the right NM, so that nonzero charge current $I_R \neq 0$ without spin-z current $I_R^{S_z} = 0$ can be detected by the right NM. For $I_R^{S_z} = 0$ nodes involving processes as mentioned above are *not* the AC-spin-interference-induced modulation nodes Q_R^* focused on here, because they originate from precession but not interference. Noteworthily, although the strict 1D ring ($M = 1$) in Fig. 2 and quasi-1D ring in Fig. 3 are both in the $M_{\text{open}} = 1$ regime, there is an essential difference between them. In Fig. 2, there are no evanescent modes, while in Fig. 3, there are two ($M - M_{\text{open}} = 3 - 1$) channels that contribute to the evanescent modes; the Q_R^* nodes in Fig. 3 are thus slightly modified from Fig. 2. Also, the $I_L^{S_z}$ can be nonzero at these Q_R^*s, simply because the FM pumps also spin-z currents directly to the left lead. To see the corresponding electric-driven results, compare Fig. 2 here with Fig. 3 in Ref. 34 and Fig. 3 here with Fig. 5 in Ref. 34.

For $M_{\text{open}} > 1$, the conducting spin states become incoherent or impure due to the entanglements between spin and orbit degrees of freedom.[34] The concept of ensemble average or spin density matrix has to be introduced to describe the transport of interferences induced by the AC effect. Furthermore, when more channels are open, the detected spin phase is obtained by taking into account the transport processes within and between each single channels, and each transport process gives different AC phases yielding different interference nodes (places where the complete destructive interference occurs); thereby, the overall complete destructive interference is washed out by different transport processes, forming the "incomplete" modulations (absence of Q_R^* nodes); for example, in Fig. 4 for $M_{\text{open}} = 2$ and $M_{\text{open}} = 3$ with $N = 200$, although one can still find the quasiperiodicity as depicted by the solid vertical lines, I_R and $I_R^{S_z}$ in general do not vanish concurrently. In addition, some of the pumped spins can be reflected in the FM|AC-ring interface before entering the AC ring, so that one has $|I_L^{S_z}| \gtrsim |I_R^{S_z}|$. To see the electric-driven case corresponding to Fig. 4, compare Fig. 4 here with Fig. 6 in Ref. 34. Note that all the above two-terminal results preserve the conservation of charge currents with $I_L = I_R$.

C. Single precessing FM island attached to four-terminal mesoscopic AC ring

In the four-terminal setup Fig. 1(a), both ISHE and AC effects emerge, giving the inverse quantum-interference-controlled SHE. As shown in Fig. 5 with the ring size $(M,N) = (1,100)$, four semi-infinite 1D probes, and $E_F = -0.05$, the transverse currents obey $I_B^{S_z} = -I_T^{S_z}$ and $I_B = I_T$ for all Q_R, signifying the ISHE. Figure 5 also shows the longitudinal currents in this four-terminal and the corresponding two-terminal setups. In the two-terminal setup, again, because of $M_{\text{open}} = 1$, the modulation nodes Q_R^* where I_R and $I_R^{S_z}$ vanish are found, rendering the complete interference modulation. In the four-terminal setup, at these Q_R^*s, although I_R and $I_R^{S_z}$ vanish as well, while the longitudinal currents, I_L and $I_L^{S_z}$, do not vanish, and the inequality $I_L \neq I_R$ shows up due to the presence of the top and bottom leads that break the longitudinal current conservation. Interestingly, the ISHE-induced Hall charge currents $I_B = I_T$ disappear at these Q_R^*s, which demonstrates again the quasiperiodicity of the modulation and is dual (satisfies the Onsager relation) to what was depicted for the SHE-induced Hall spin currents (in the form of spin-Hall conductance) in Fig. 2 of Ref. 35. Also note that transverse currents I_B and I_T decrease as increasing Q_R due to the reflections in the interfaces between the AC ring and the top or bottom leads, a manifestation of the lattice Hamiltonian mismatch.

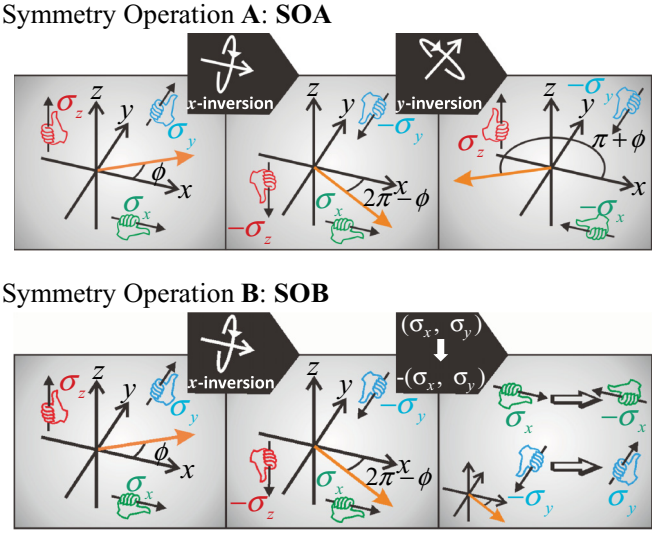

FIG. 9. (Color online) Symmetry operations **A** (SOA) and **B** (SOB). In SOA, the inversion with respect to the $+x$ axis (as depicted by the inset, x inversion) is first performed to the system represented by the orange/gray arrow lying on the x-y plane and then with respect to the $+y$ axis (as depicted by the inset, y inversion). In SOB, x inversion is first performed and then the replacement $(\sigma_x,\sigma_y) \rightarrow -(\sigma_x,\sigma_y)$. The successive figures show how the spin $(\sigma_x,\sigma_y,\sigma_z)$ and polar angle ϕ change after each inverting or replacing.

To see how the width of the ring M affects the interference, we consider the AC ring with fixed $N = 100$ in contact with four semi-infinite 1D leads such that only one channel is available for transport in each lead, i.e., $M_{\text{open}} = 1$. Figure 6 indicates that the modulation frequency of the Hall currents $I_B = I_T$ for $M = 2$ is almost double to that for $M = 1$, because in $M = 2$, one additional transport ring path appears. For larger width, the oscillations of Hall currents become vague since the multiple intertwined 1D ring paths smear out the periodic behavior of the currents or average over the AC phase; nevertheless, the complete quasiperiodicity ($I_B = I_T = 0$ at current modulation nodes Q_R^*) is protected by the $M_{\text{open}} = 1$ condition. The reciprocal features (for the corresponding electric-driven setup) are shown in Fig. 3 of Ref. 35. Note that the ISHE emerging through $I_B^{S_z} = -I_T^{S_z}$ and $I_B = I_T$ is still preserved robustly against the ring width.

Interestingly, the ISHE remains unaffected even in the weak-disorder regime. Figure 7 plots the probed currents with different (weak) disorder strength W modeled by the random on-site potentials of the ring, namely, $\varepsilon^{n,m} \in [-W/2, W/2]$. The modulations of $I_B^{S_z} = -I_T^{S_z}$ and $I_B = I_T$ show that ISHE is robust against weak disorder. In addition, the presence of the weak disorder plays merely the role of reducing the amplitudes of the modulation as also addressed in Ref. 35 for the corresponding electric-driven setup (compare Fig. 7 here with Fig. 4 in Ref. 35).

D. Symmetry operations relating pumped spin and charge currents

We extend our study to the case of multiple precessing FM islands and examine the relations between the pumped currents. Consider the two-terminal setup Fig. 1(b) with an additional FM island inserted between the ring and the right NM (as the schematics shown in Fig. 10). Let Θ_R (Θ_L) be the precession cone angle and Φ_R (Φ_L) be the initial precession phase of the right (left) FM. For $M_{\text{open}} = 1$ at the condition $Q_R \approx Q_R^*$, we find that the spin-z currents probed by the left (right) lead remain almost constant when varying Θ_R (Θ_L) and/or Φ_R (Φ_L); in other words, the left FM does not communicate with the right FM due to the complete destructive interference. Contrarily, in Fig. 8, with $E_F = -1.8$, $(M, N) = (1, 200)$ ring, two (left and right) 1D leads, fixed $\Theta_L = 10^\circ$ (indicated by the dashed line) and $\Phi_L = 0^\circ$ in the left FM, at $Q_R = 5$, i.e., the condition of the complete destructive interference is off, we see that the pumped currents probed by the left lead, I_L, $I_L^{S_x}$, $I_L^{S_y}$, and $I_L^{S_z}$, significantly change with Θ_R . For Φ_R dependence, noteworthily, we see that I_L and $I_L^{S_z}$ are not as sensitive to Φ_R as $I_L^{S_x}$ and $I_L^{S_y}$ (for example, compare panels of Fig. 8 at $\Theta_R \approx 135^\circ$).

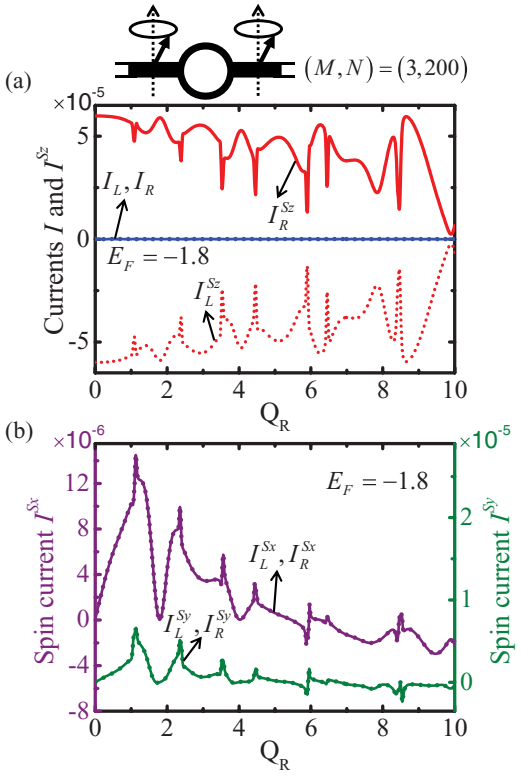

FIG. 10. (Color online) Pumped (a) charge and spin-z currents and (b) spin-x and spin-y currents probed by the left and right leads of finite width consisting of three lattice points versus the dimensionless Rashba spin-orbit coupling strength Q_R in the two-terminal two-precessing-FM setup P_{10°-P_{10° (top schematics); i.e., the left ferromagnet and right ferromagnet are of precession cone angle 10° and precession axes both along the $+z$ direction.

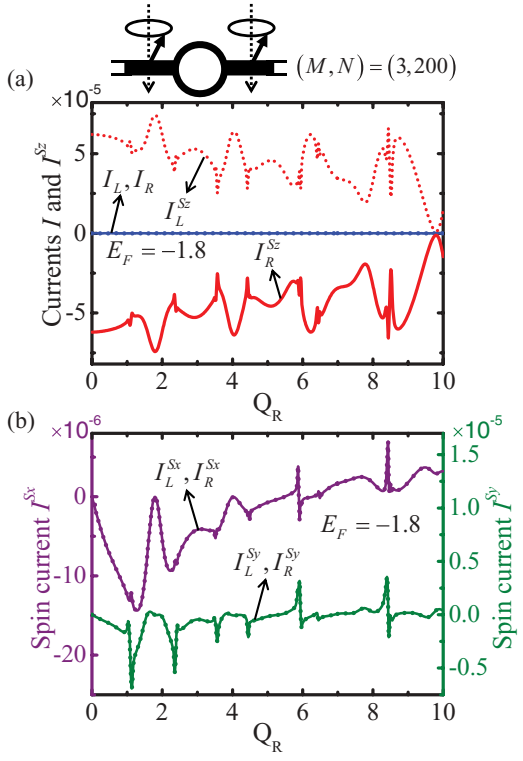

FIG. 11. (Color online) Pumped (a) charge and spin-z currents and (b) spin-x and spin-y currents versus the dimensionless Rashba spin-orbit coupling strength Q_R in the two-precessing-FM setup $\bar{P}_{10^\circ}$-$\bar{P}_{10^\circ}$ (top schematics) the same as the one considered in Fig. 10 but with precession axes along the $-z$ direction for both the left and right ferromagnets.

To establish a systematic analysis on the relations between pumped currents, we inspect the device from the symmetry perspective. Recall that the Rashba SOC originates from the structural inversion asymmetry,[60] meaning that the AC ring Hamiltonian, Eq. (2) defined by Eqs. (3) and (4), does not remain the same by inverting the ring once. This one-time inversion asymmetry, however, leads to the conjecture that if one can somehow perform some inversion-like operations twice, then $H_{\rm ACR}$ might be invariant. Indeed, at least two types of symmetry operations can render invariant $H_{\rm ACR}$. These two operations are illustrated in Fig. 9. We refer to the first operation as symmetry operation **A** (abbreviated as SOA), and the second as symmetry operation **B** (abbreviated as SOB). In SOA, we first invert the system with respect to the $+x$ axis (x inversion) and then invert again with respect to the $+y$ axis (y inversion); note that each inversion gives a $\Delta\phi \to -\Delta\phi$ and a $\sigma_z \to -\sigma_z$. After these two inversions, as shown in Fig. 9 we have $\phi \to \pi + \phi$, $\Delta\phi \to \Delta\phi$, and

$$(\sigma_x,\sigma_y,\sigma_z) \to (-\sigma_x,-\sigma_y,\sigma_z), \quad \text{for} \quad \text{SOA}, \tag{37}$$

such that Eqs. (3) and (4) remain unaltered, conceding invariant $H_{\rm ACR}$. For SOB, we first perform the x inversion and then the replacement $(\sigma_x,\sigma_y) \to -(\sigma_x,\sigma_y)$; note that in SOB, the σ_y undergoes $\sigma_y \to -\sigma_y \to \sigma_y$ ($\sigma_y \to -\sigma_y$ due to the inversion and then $-\sigma_y \to \sigma_y$ due to the replacement). We thus get (refer to Fig. 9), $\phi \to 2\pi - \phi$, $\Delta\phi \to -\Delta\phi$, and

$$(\sigma_x,\sigma_y,\sigma_z) \to (-\sigma_x,\sigma_y,-\sigma_z), \quad \text{for} \quad \text{SOB}, \tag{38}$$

so that Eqs. (3) and (4) are unchanged to yield invariant $H_{\rm ACR}$ as well.

For NMs, obviously, after SOA or SOB, the $H_{\rm NM}$ remains the same, because all NMs are of the same spin-independent structural-inversion-invariant Hamiltonian. Also, all the hybridizations (characterized by the same spin-independent hopping $-\gamma_0$), $H_{\text{NM-ACR}}$, $H_{\text{FM-ACR}}$, and $H_{\text{FM-NM}}$ are SOA and SOB invariant. The only portion in the total Hamiltonian that might not be able to recover to its original form is the time-dependent Hamiltonian $H_{\rm FM}(t)$, because under SOA or SOB the directions of the precession axis can vary. However, note that since what we are interested in is the *time-averaged* currents, it is the *relative* initial precessing phase $\Phi_L - \Phi_R$ that is relevant to these average currents, while the $\Phi_L - \Phi_R$ does not change under SOA or SOB, because SOA or SOB is applied to the whole system (i.e., to all precessing FMs). Moreover, any operations or transformations will transfer one pumping configuration either to the same configuration or to another configuration; in the former, the symmetry argument will relate the probed pumped currents within a single configuration, whereas in the latter, it will relate the probed currents between two different configurations; this will become more clear in the next section. Without loss of generality, in what follows, we

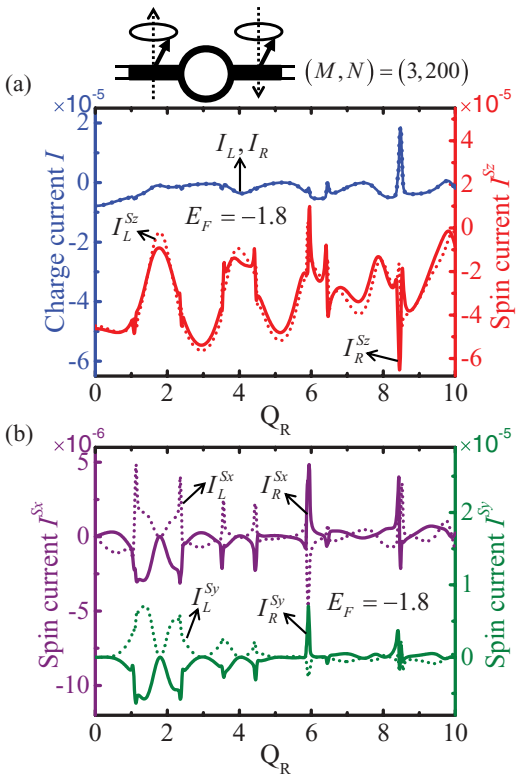

FIG. 12. (Color online) Pumped (a) charge and spin-z currents and (b) spin-x and spin-y currents versus the dimensionless Rashba spin-orbit coupling strength Q_R in the two-precessing-FM setup P_{10°-$\bar{P}_{10^\circ}$ (top schematics) the same as the one considered in Fig. 10 but with precession axis along the $+z$ ($-z$) direction for the left (right) ferromagnet.

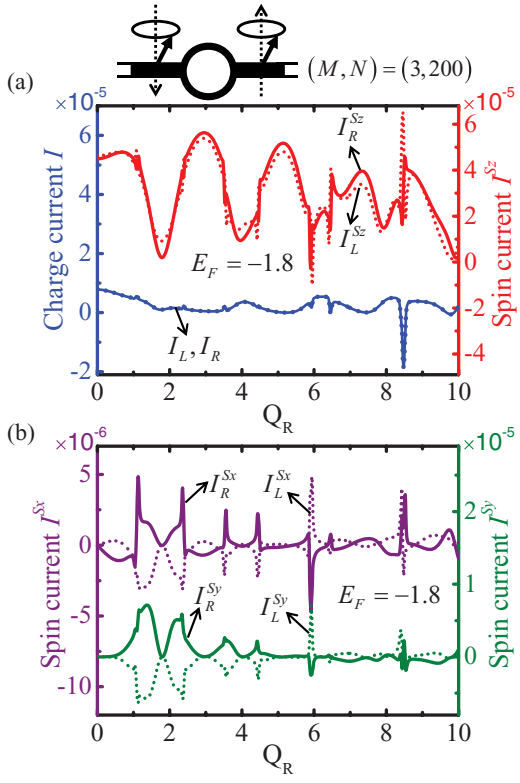

FIG. 13. (Color online) Pumped (a) charge and spin-z currents and (b) spin-x and spin-y currents versus the dimensionless Rashba spin-orbit coupling strength Q_R in the two-precessing-FM setup $\bar{P}_{10^\circ}$-P_{10° (top schematics) the same as the one considered in Fig. 10 but with precession axis along the $-z$ ($+z$) direction for the left (right) ferromagnet.

choose systems originally at $\Phi_L = \Phi_R = 0^\circ$ to illustrate how SOA or SOB helps construct the relations between different probed currents and verify these relations by inspecting our numerical results.

E. Symmetry arguments applied to two precessing FM islands with two-terminal mesoscopic AC ring in between

For the purpose of demonstration, we choose to consider here the two-terminal two-precessing-FM (left and right FMs adjacent to the left and to the right of the ring, respectively) setups, while one can apply the argument presented below also to the ring devices consisting of an arbitrary number of terminals and precessing FM islands. In addition, since the definitions of SOA and SOB have nothing to do with the ring width M, ring length N, number of open channels $M_{\rm open}$, and E_F, *the symmetry argument is valid for any* $M, N, M_{\rm open}$, *and* E_F. Here, we choose $(M,N) = (3,200)$ and set $E_F = -1.8\gamma_0$ giving $M_{\rm open} = 2$ to exemplify the symmetry operations. We use the notation convention A-B to describe the pumping configuration, with A accounting for the left precessing FM and B for the right precessing FM. Here, with $\{A, B\} \in \{P_\Theta, \bar{P}_\Theta\}$, P_Θ ($\bar{P}_\Theta$) stands for the FM that is of precession axis along the $+z$ ($-z$) axis and of precession cone angle Θ. For example, the schematics in Fig. 10 is notated as P_{10°-P_{10°, in Fig. 12 as P_{10°-$\bar{P}_{10^\circ}$, and in Fig. 17 as $\bar{P}_{90^\circ}$-P_{90°.

Focus on SOA first. Consider P_{10°-P_{10°, Fig. 10. By applying SOA to P_{10°-P_{10°, the first step (x inversion) generates $\bar{P}_{170^\circ}$-$\bar{P}_{170^\circ}$, while the second step (y inversion) yields the swap L (left) $\leftrightarrow$ R (right) and turns $\bar{P}_{170^\circ}$-$\bar{P}_{170^\circ}$ into P_{10°-P_{10°; i.e., the original pumping configuration is recovered. As a result, in P_{10°-P_{10° we have, due to the y inversion involved in SOA, $I_L = -I_R$ (or $I_L^{S_q} = -I_R^{S_q}$ for all q components before any operations on spins), which then incorporated with the replacement (37) turns $I_L^{S_q} = -I_R^{S_q}$ into $(I_L^{S_x}, I_L^{S_y}, I_L^{S_z}) = (I_R^{S_x}, I_R^{S_y}, -I_R^{S_z})$, in line with our numerical result, Fig. 10. In Fig. 11 ($\bar{P}_{10^\circ}$-$\bar{P}_{10^\circ}$), by employing the same argument based on SOA, we obtain again the relations $I_L = -I_R$ and $(I_L^{S_x}, I_L^{S_y}, I_L^{S_z}) = (I_R^{S_x}, I_R^{S_y}, -I_R^{S_z})$. It is noteworthy that in the pumping configuration A-A such as in Figs. 10 and 11, the probed charge currents vanish $I_L = I_R = 0$ due to the left-right transmission symmetry,[49] resulting in *pure* spin currents in the NMs; this absence of charge currents can also be obtained by noting that the current conservation $I_L = I_R$ and the symmetry argument that gives $I_L = -I_R$ have to be satisfied simultaneously.

On the other hand, for the left-right transmission asymmetric cases such as Figs. 12 (P_{10°-$\bar{P}_{10^\circ}$) and 13 ($\bar{P}_{10^\circ}$-P_{10°), I_L and I_R in general can be nonzero. Similarly, performing SOA on P_{10°-$\bar{P}_{10^\circ}$ ($\bar{P}_{10^\circ}$-P_{10°), the x inversion renders $\bar{P}_{170^\circ}$-P_{170° (P_{170°-$\bar{P}_{170^\circ}$), and then the proceeding y inversion gives $\bar{P}_{10^\circ}$-P_{10° (P_{10°-$\bar{P}_{10^\circ}$); hence, SOA transfers P_{10°-$\bar{P}_{10^\circ}$

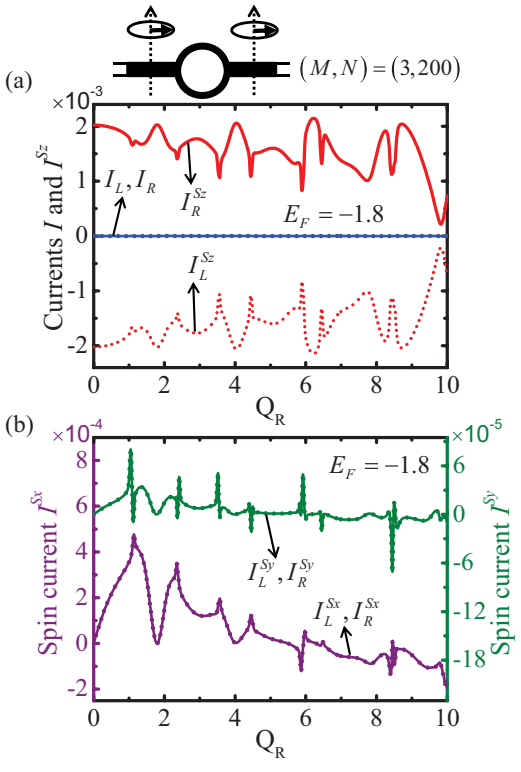

FIG. 14. (Color online) Pumped (a) charge and spin-z currents and (b) spin-x and spin-y currents probed by the left and right leads of finite width consisting of three lattice points versus the dimensionless Rashba spin-orbit coupling strength Q_R in the two-terminal two-precessing-FM setup P_{90°-P_{90° (top schematics); i.e., both the left and right ferromagnets are of precession cone angle 90° and precession axis along the $+z$ direction.

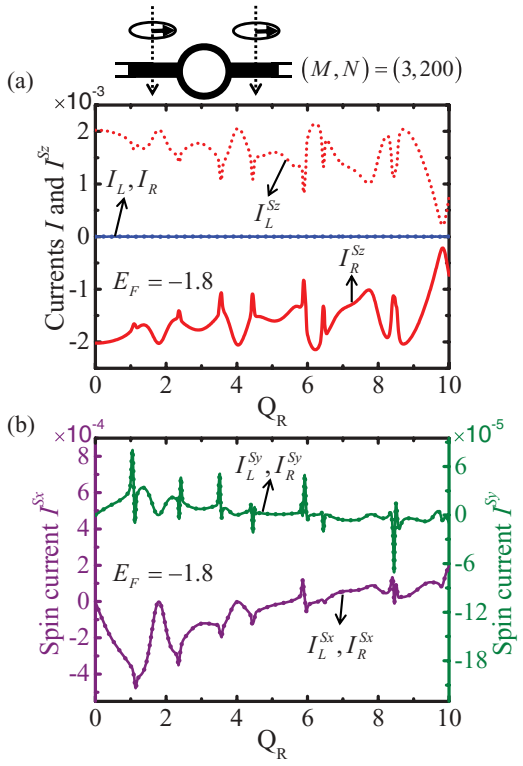

FIG. 15. (Color online) Pumped (a) charge and spin-z currents and (b) spin-x and spin-y currents versus the dimensionless Rashba spin-orbit coupling strength Q_R in the two-precessing-FM setup $\bar{P}_{90^\circ}$-$\bar{P}_{90^\circ}$ (top schematics) the same as the one considered in Fig. 14 but with precession axis along the $-z$ direction for both left and right ferromagnets.

($\bar{P}_{10^\circ}$-P_{10°) to the different pumping configuration $\bar{P}_{10^\circ}$-P_{10° (P_{10°-$\bar{P}_{10^\circ}$). Therefore, the current $I_{L;R}$ in P_{10°-$\bar{P}_{10^\circ}$ ($\bar{P}_{10^\circ}$-P_{10°) equals $-I_{R;L}$ in $\bar{P}_{10^\circ}$-P_{10° (P_{10°-$\bar{P}_{10^\circ}$). Again, the relations above for charge currents together with the replacement (37) make $(I_L^{S_x}, I_L^{S_y}, I_L^{S_z})$ in P_{10°-$\bar{P}_{10^\circ}$ ($\bar{P}_{10^\circ}$-P_{10°) identical to $(I_R^{S_x}, I_R^{S_y}, -I_R^{S_z})$ in $\bar{P}_{10^\circ}$-P_{10° (P_{10°-$\bar{P}_{10^\circ}$) and $(I_R^{S_x}, I_R^{S_y}, I_R^{S_z})$ in P_{10°-$\bar{P}_{10^\circ}$ ($\bar{P}_{10^\circ}$-P_{10°) identical to $(I_L^{S_x}, I_L^{S_y}, -I_L^{S_z})$ in $\bar{P}_{10^\circ}$-P_{10° (P_{10°-$\bar{P}_{10^\circ}$). All above features are again in line with our numerical results, Fig. 12 and Fig. 13. It should be noted here that $\Theta = 10^\circ$ in our numerical calculation is chosen merely for the illustrations of symmetry operations. The symmetry argument presented above in fact is applicable for any cone angle Θ and even for the case of $\Theta_L \neq \Theta_R$; i.e., the precessing cone angles for left (Θ_L) and right (Θ_R) FMs are different. Particularly, at $\Theta = \Theta_L = \Theta_R = 90^\circ$, all the relations based on SOA shown above are preserved as well (see Figs. 14–17), while since the pumping configuration for $\Theta = 90^\circ$ (precession within the two-dimensional x-y plane) is of higher geometrical symmetry than $\Theta = 10^\circ$, the probed currents are of additional relations as demonstrated below.

Following the same procedure presented above, one can also apply SOB to any A-B configuration to relate probed currents in a single pumping configuration (if SOB does not generate another pumping configuration) or to relate probed currents between different pumping configurations (if SOB generates another pumping configuration). Here, we choose to focus on the special case with $\Theta = 90^\circ$. Unlike the case of $\Theta = 10^\circ$ where we have no relations of the pumped currents between the two different pumping configurations, P_{10°-P_{10° and $\bar{P}_{10^\circ}$-$\bar{P}_{10^\circ}$, at $\Theta = 90^\circ$ the pumped currents in P_{90°-P_{90° can relate to the pumped currents in $\bar{P}_{90^\circ}$-$\bar{P}_{90^\circ}$. Applying SOB to P_{90°-P_{90° (Fig. 14) yields $\bar{P}_{90^\circ}$-$\bar{P}_{90^\circ}$ (Fig. 15) so that $I_{L(R)}$ in P_{90°-P_{90° is equal to $I_{L(R)}$ in $\bar{P}_{90^\circ}$-$\bar{P}_{90^\circ}$. This relation, again, incorporated with the replacement (38) leads to the spin current $(I_{L(R)}^{S_x}, I_{L(R)}^{S_y}, I_{L(R)}^{S_z})$ in P_{90°-P_{90° equal to the spin current $(-I_{L(R)}^{S_x}, I_{L(R)}^{S_y}, -I_{L(R)}^{S_z})$ in $\bar{P}_{90^\circ}$-$\bar{P}_{90^\circ}$. The above predictions agree with our numerical results, Figs. 14 and 15. It is worth noting that although P_{10°-P_{10°, $\bar{P}_{10^\circ}$-$\bar{P}_{10^\circ}$, P_{90°-P_{90°, and $\bar{P}_{90^\circ}$-$\bar{P}_{90^\circ}$ all generate *net* pure in-plane (x-y plane) spin currents, i.e., $I_L + I_R = I_L^{S_z} + I_R^{S_z} = 0$ as predicted by SOA, the pumped spin currents at $\Theta = 90^\circ$ are one to two orders larger than those at $\Theta = 10^\circ$ (compare Figs. 10 and 11 with Figs. 14 and 15). Similar enhancement of the pumped spin currents by the cone angle can also be found by comparing Figs. 12 (P_{10°-$\bar{P}_{10^\circ}$) and 13 ($\bar{P}_{10^\circ}$-P_{10°) with Figs. 16 (P_{90°-$\bar{P}_{90^\circ}$) and 17 ($\bar{P}_{90^\circ}$-P_{90°). The additional (beside what were obtained by SOA) relations between P_{90°-$\bar{P}_{90^\circ}$ and $\bar{P}_{90^\circ}$-P_{90° can be obtained by performing SOB. Applying SOB to P_{90°-$\bar{P}_{90^\circ}$ (Fig. 16), we arrive at $\bar{P}_{90^\circ}$-P_{90° (Fig. 17), with $I_{L(R)}$ in P_{90°-$\bar{P}_{90^\circ}$ equal to $I_{L(R)}$ in $\bar{P}_{90^\circ}$-P_{90°, and then, by replacement (38), $(I_{L(R)}^{S_x}, I_{L(R)}^{S_y}, I_{L(R)}^{S_z})$ in P_{90°-$\bar{P}_{90^\circ}$ equal to

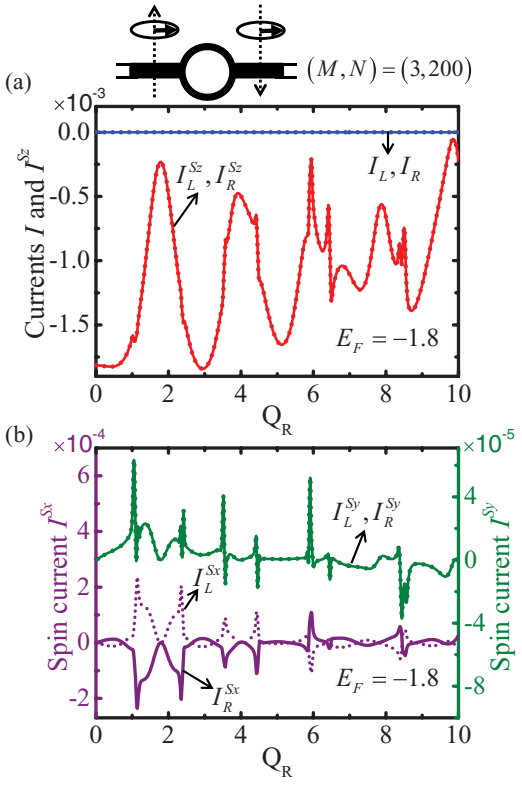

FIG. 16. (Color online) Pumped (a) charge and spin-z currents and (b) spin-x and spin-y currents versus the dimensionless Rashba spin-orbit coupling strength Q_R in the two-precessing-FM setup P_{90°-$\bar{P}_{90^\circ}$ (top schematics) the same as the one considered in Fig. 14 but with precession axis along the $+z$ ($-z$) direction for the left (right) ferromagnet.

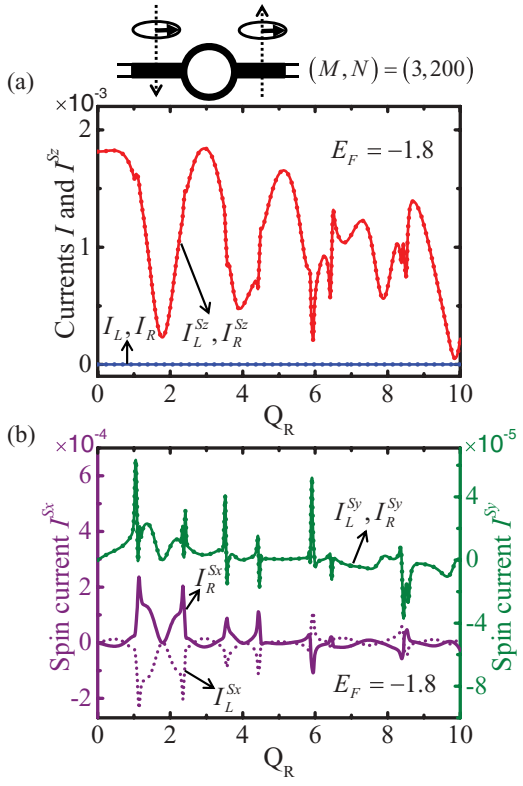

FIG. 17. (Color online) Pumped (a) charge and spin-z currents and (b) spin-x and spin-y currents versus the dimensionless Rashba spin-orbit coupling strength Q_R in the two-precessing-FM setup $\bar{P}_{90^\circ}$-P_{90° (top schematics) the same as the one considered in Fig. 14 but with precession axis along the $-z$ ($+z$) direction for the left (right) ferromagnet.

$(-I^{S_x}_{L(R)}, I^{S_y}_{L(R)}, -I^{S_z}_{L(R)})$ in $\bar{P}_{90^\circ}$-P_{90°, in line with Figs. 16 and 17. We note that for all $\Theta = 90^\circ$ pumping configurations, the pumped spin currents are pure (namely, $I_L = I_R = 0$); this again can be achieved by considering the current conservation together with the symmetry argument based on SOA and SOB. We emphasize that our results here show that the current polarization direction can be tuned by the top-gate voltage governing Q_R, and the magnitude of the pumped currents can be controlled by the precession cone angle Θ, offering amenable manipulations on the output currents from the proposed device.

V. CONCLUSION

In conclusion, by introducing the auxiliary system where the time domain is treated effectively as an additional real-space degree of freedom, we offer a plain access to the Floquet-NEGF formalism capable of dealing with time-periodic dynamic problems in a full quantum approach. Particularly, by further adopting the reduced-zone scheme,[38] we derived expressions (32)–(35) in which charge currents are conserved for any given maximum number of photons as shown in the Appendix, where comparisons with other existing results are also provided. With the help of Eqs. (34) and (35), we reveal the physics attributed to the AC effect by considering the ring of Rashba SOC in spin-driven four- [Fig. 1(a)] and two-terminal [Fig. 1(b)] setups.

When the number of open channel in the leads is one, $M_{\text{open}} = 1$, as a consequence of the AC effect, the complete AC-spin-interference-induced modulation nodes characterized by $I_R = I^{S_z}_R = 0$ at certain Rashba SOC strengths Q^*_R (where the complete destructive interferences occur) are found to be independent of the Fermi energy E_F in both two- and four-terminal cases (Figs. 2, 3, and 5). We note that the form of Eqs. (32)–(35) remains the same in the presence of Coulomb interactions, and one can preserve the conservation of the charge current within the framework of NEGF by treating each physical lead as $2n^{\max}_{\text{ph}} + 1$ photon-associated leads (refer to the Appendix). However, depending on the Fermi energy, magnetic states can be formed due to the Coulomb interactions.[61,62] One may then expect that the Fermi energy independent property of the Q^*_Rs only holds in the regime where those magnetic states do not appear (for example, large ratio between the level broadening and the strength of the Coulomb interaction and/or smaller Fermi energy than the on-site potentials of the ring) so that electrons traveling through the ring do not encounter those scattering which can yield additional spin-dependent phases.

In the four-terminal setup, the interference modulation is also characterized by $I_B = I_T = 0$ at the corresponding two-terminal Q^*_Rs (i.e., Fig. 5, top panel $I_R = I^{S_z}_R = 0$ and bottom panel $I_B = I_T = 0$ vanish at the same Q^*_Rs). Increasing the number of open channels by tuning the Fermi energy to reach the $M_{\text{open}} > 1$ regime in quasi-1D (of finite width) rings destroys the completeness of the modulation, i.e., absence of Q^*_R (Fig. 4). Nevertheless, in the four-terminal case, we find that the ISHE identified by $I_B = I_T$ and $I^{S_z}_B + I^{S_z}_T = 0$ (Fig. 5, bottom panel) is robust against the ring width (Fig. 6) and weak disorder (Fig. 7), and therefore, the proposed device offers a durable electrical means to measure the pure spin currents pumped by the precessing FM islands using the inverse quantum-interference-controlled SHE in the AC rings. The above features based on our spin-driven setups reciprocally well correspond to the findings in the electric-driven setup, Refs. 34 and 35, supporting our derived formalism.

In addition to the single-precessing-FM setup (Fig. 1), a multiple-precessing-FM setup is studied. In the two-terminal two-precessing-FM setup where the ring is in contact with two (left and right) precessing FM islands, we find that the currents probed by the left (right) lead are independent of Θ_R and Φ_R (Θ_L and Φ_L) of the right (left) FM under the condition of complete destructive interferences. In other words, the complete destructive interference blocks out the relation between the left portion (left FM and left lead) and the right portion (right FM and right lead) of our device, while this relation revives when the condition of the destructive interference is suppressed (Fig. 8).

We also identified two symmetry operations, SOA and SOB (Fig. 9), to examine the relations between currents in the same pumping configurations or different configurations. Performing SOA or SOB on an arbitrary pumping configuration together with the fact that charge currents should be conserved, one can first relate the charge currents either in the same or in different pumping configurations, and then using Eq. (37) for SOA or Eq. (38) for SOB, one can further obtain the relations between spin currents. We choose to exemplify how the above procedure works by considering the two-terminal two-precessing-FM setup with precession cone angles $\Theta_L = \Theta_R = 10^\circ$ (Figs. 10–13) and $\Theta_L = \Theta_R = 90^\circ$ (Figs. 14–17). The relations predicted by SOA and SOB are consistent with our numerical results. Especially, the net pure in-plane spin currents (for x-y plane with $I_L + I_R = I^{S_z}_L + I^{S_z}_R = 0$ in Figs. 10, 11, 14, and 15, and for y-z plane with $I_L + I_R = I^{S_x}_L + I^{S_x}_R = 0$ in Figs. 16 and 17) can be achieved, and for all $\Theta_L = \Theta_R = 90^\circ$ pumping configurations, the pumped spin currents are pure, namely, $I_L = I_R = 0$. Therefore, with employing the spin-pumping device proposed here, the pumped currents can be controlled with their magnitudes and polarization directions tunable via the pumping configurations (including the precessing cone angle) and the applied top-gate voltage that varies Q_R), giving potential applications in spintronics-based industry.

ACKNOWLEDGMENTS

S.-H.C., C.-L.C., and C.-R.C. gratefully acknowledge financial support by the Republic of China National Science Council Grant No. NSC98-2112-M-002-012-MY3. F.M. is supported by DOE Grant No. DE-FG02-07ER46374. One of the authors, S.-H.C., would like to thank Branislav K. Nikolić for his valuable stimulating discussions and suggestions.

APPENDIX: CONSERVATION OF CHARGE CURRENT BY REDUCED-ZONE SCHEME

To derive and have some insights into the conservation of charge current, we introduce the photon-associated lead (or simply photon lead) λ which accounts for the physical lead index p and the photon index n_{ph}. In other words, we regards

each lead p now as consisting of $(2n_{\rm ph}+1)$ photon leads. The sum over p on Eq. (34), $\sum_p \mathrm{sign}(p) I_p$, can then be written as

$$\sum_{\lambda,\lambda'}\int_{E_F-\hbar\omega/2}^{E_F+\hbar\omega/2} dE\,\mathrm{Tr}[\check{G}^r(E)\check{f}^{(\lambda')}(E)\check{\Gamma}^{(\lambda')}(E)\check{G}^a(E)\check{\Gamma}^{(\lambda)}(E) - \check{G}^r(E)\check{\Gamma}^{(\lambda')}(E)\check{G}^a(E)\check{f}^{(\lambda)}(E)\check{\Gamma}^{(\lambda)}(E)]. \quad \text{(A1)}$$

Using the cyclic relation $\mathrm{Tr}(ABC)=\mathrm{Tr}(BCA)=\mathrm{Tr}(CAB)$, Eq. (A1) becomes

$$\sum_{\lambda,\lambda'}\int_{E_F-\hbar\omega/2}^{E_F+\hbar\omega/2} dE\,\mathrm{Tr}[\check{G}^a(E)\check{\Gamma}^{(\lambda)}(E)\check{G}^r(E)\check{f}^{(\lambda')}(E)\check{\Gamma}^{(\lambda')}(E) - \check{G}^r(E)\check{\Gamma}^{(\lambda')}(E)\check{G}^a(E)\check{f}^{(\lambda)}(E)\check{\Gamma}^{(\lambda)}(E)]. \quad \text{(A2)}$$

Summing over λ, the first term in Eq. (A2) reads

$$\sum_{\lambda'}\int_{E_F-\hbar\omega/2}^{E_F+\hbar\omega/2} dE\,\mathrm{Tr}\check{G}^a(E)\check{\Gamma}(E)\check{G}^r(E)\check{f}^{(\lambda')}(E)\check{\Gamma}^{(\lambda')}(E), \quad \text{(A3)}$$

while summing over λ', the second term reads

$$\sum_{\lambda}\int_{E_F-\hbar\omega/2}^{E_F+\hbar\omega/2} dE\,\mathrm{Tr}\,\check{G}^r(E)\check{\Gamma}(E)\check{G}^a(E)\check{f}^{(\lambda)}(E)\check{\Gamma}^{(\lambda)}(E), \quad \text{(A4)}$$

with $\check{\Gamma}\equiv\sum_\lambda\check{\Gamma}^{(\lambda)}=\sum_{p,n_{\rm ph}}-2|\gamma_0|^2\mathrm{Im}\check{g}^{(p)r}_{n_{\rm ph},n_{\rm ph}}=[(\check{G}^r)^{-1}-(\check{G}^a)^{-1}]/i$. Renaming λ' in Eq. (A3) as λ for λ' is a dummy variable and using the equality $\check{G}^a(E)\check{\Gamma}(E)\check{G}^r(E)=\check{G}^r(E)\check{\Gamma}(E)\check{G}^a(E)=(\check{G}^a-\check{G}^r)/i$, we find that the two terms Eqs. (A3) and (A4) are equal; i.e., they cancel out with each other in Eq. (A2). We thus arrive at the conservation of charge current, $\sum_p \mathrm{sign}(p) I_p=0$. The derivation presented above can be applied to Eq. (32) as well to show the conservation $\sum_p I_p(t)=0$ at any given time t.

The physical picture of the conservation becomes transparent by noting also that Eq. (A1) can be written as

$$\sum_{\lambda,\lambda'}\int_{E_F-\hbar\omega/2}^{E_F+\hbar\omega/2} dE\,\mathrm{Tr}[\check{G}^r(E)\check{\Gamma}^{(\lambda')}(E)\check{G}^a(E)\check{\Gamma}^{(\lambda)}(E)] \times[\check{f}^{(\lambda')}(E)-\check{f}^{(\lambda)}(E)],$$

which recovers the conventional expression of the charge current flowing into a photon lead λ,

$$I_\lambda=\frac{1}{2\pi\hbar}\sum_{\lambda'}\int_{E_F-\hbar\omega/2}^{E_F+\hbar\omega/2} dE\,\mathrm{Tr}[\check{G}^r(E)\check{\Gamma}^{(\lambda')}(E)\check{G}^a(E)\check{\Gamma}^{(\lambda)}(E)] \times[\check{f}^{(\lambda')}(E)-\check{f}^{(\lambda)}(E)], \quad \text{(A5)}$$

that gives the conservation $\sum_\lambda I_\lambda=0$. Consider for instance a two-terminal case with $p=L$ or R. In practice (numerical calculation), we choose a maximum $n_{\rm ph}^{\rm max}\geqslant|n_{\rm ph}|$. Taking $n_{\rm ph}^{\rm max}=2$ for example, we have now $2n_{\rm ph}^{\rm max}+1=5$ photon leads for each left $p=L$ and right $p=R$ physical lead. When computing the current flowing through the left lead with employing the reduced-zone scheme using Eq. (34) or equivalently Eq. (A5) by $\sum_{\lambda=L_{-2},\,L_{-1},L_0,L_1,L_2} I_\lambda$, the five left photon leads (sources) $\lambda=(p=L)_{n_{\rm ph}=-2}$, L_{-1}, L_0, L_1, and L_2 and the five right photon leads (drains) $\lambda'=R_{-2}$, R_{-1}, R_0, R_1, and R_2 are taken into account. The same symmetric (i.e., all sources become drains, and all drains become sources) photon lead geometry is used when computing, again by Eq. (34) with the same $n_{\rm ph}^{\rm max}=2$, the current flowing through right lead.

Accordingly, this *symmetric photon lead geometry* provided by the reduced-zone scheme yields the conservation of the charge current; while practically we increase $n_{\rm ph}^{\rm max}$ until the difference between the results obtained by $n_{\rm ph}^{\rm max}$ and by $n_{\rm ph}^{\rm max}+1$ is within certain tolerance (small number), *the conservation in fact holds for any given* $n_{\rm ph}^{\rm max}$, because the geometry symmetry of all photon leads introduced by the physical leads is preserved at any approximate levels of the accounted number of photons.

Contrarily, without using the reduced-zone scheme, Eq. (34) becomes, by "unfolding" the energy E, $\sum_{n_{\rm ph}}\int_{E_F-\hbar\omega/2}^{E_F+\hbar\omega/2} dE\,\mathrm{Tr}\,(\cdots)\longrightarrow\int_{-\infty}^{\infty} dE\,\mathrm{Tr}(\cdots)_{n_{\rm ph}=0,n_{\rm ph}=0}$,

$$\mathrm{sign}(p)\sum_{p'}\sum_{n_{\rm ph}}\int_{-\infty}^{\infty} dE\,\mathrm{Tr}\big\{[\check{G}^r(E)]_{0,n_{\rm ph}}[\check{\Gamma}^{(p')}(E)]_{n_{\rm ph},n_{\rm ph}} \times[\check{G}^a(E)]_{n_{\rm ph},0}[\check{\Gamma}^{(p)}(E)]_{0,0}\big\} \times\big\{[\check{f}^{(p')}(E)]_{n_{\rm ph},n_{\rm ph}}-[\check{f}^{(p)}(E)]_{0,0}\big\}, \quad \text{(A6)}$$

which reduces to the conventionally well-known expression.[43,51,63–71] Nevertheless, the conservation is practically difficult to be satisfied due to the *asymmetric photon lead geometry* by Eq. (A6). We take again the two-terminal case ($p=L$ or R) with choosing $n_{\rm ph}^{\rm max}=2$ for example. At a given energy E, using Eq. (A6) to compute $I_{p=L}$, the photon lead geometry is L_0 as the source and L_{-2}, L_{-1}, L_1, L_2, R_{-2}, R_{-1}, R_0, R_1, R_2 as the drains, while the same Eq. (A6) used to compute $I_{p=R}$ takes into account the asymmetric photon lead geometry, R_0 as the source and R_{-2}, R_{-1}, R_1, R_2, R_{-2}, L_{-1}, L_0, L_1, L_2 as the drains. The asymmetry implies that current following through R_0 in general is not equal to the current flowing through L_0, which manifests also via the asymmetric transmission between the left and right leads,[70] and thus fails to fulfill the conservation.

It is worth mentioning that in the case of the same unbiased leads, $\check{f}^{(p)}(E)=\check{f}^{(p')}(E)\equiv\check{f}(E)$, the symmetric photon lead geometry ensuring the conservation can be restored by symmetrically adding the other photon channels $m_{\rm ph}$ to Eq. (A6); i.e., one can write I_p as

$$\frac{\mathrm{sign}(p)}{2n_{\rm ph}^{\rm max}}\sum_{p'}\sum_{n_{\rm ph},m_{\rm ph}}\int_{-\infty}^{\infty} dE\,\mathrm{Tr}\big\{[\check{G}^r(E)]_{m_{\rm ph},n_{\rm ph}} \times[\check{\Gamma}^{(p')}(E)]_{n_{\rm ph},n_{\rm ph}}[\check{G}^a(E)]_{n_{\rm ph},m_{\rm ph}}[\check{\Gamma}^{(p)}(E)]_{m_{\rm ph},m_{\rm ph}}\big\} \times\big\{[\check{f}(E)]_{n_{\rm ph},n_{\rm ph}}-[\check{f}(E)]_{m_{\rm ph},m_{\rm ph}}\big\}. \quad \text{(A7)}$$

Notice that the original summation $\sum_{n_{\rm ph}}$ takes into account $(2n_{\rm ph}^{\rm max}+1)$ photon channels, while now the summation $\sum_{n_{\rm ph},m_{\rm ph}}$ above takes into account, noting that $m_{\rm ph}=n_{\rm ph}$ does not give contributions because of the factor $[\check{f}(E)]_{n_{\rm ph},n_{\rm ph}}-[\check{f}(E)]_{m_{\rm ph},m_{\rm ph}}$, $(2n_{\rm ph}^{\rm max}+1)\times(2n_{\rm ph}^{\rm max}+1)-(2n_{\rm ph}^{\rm max}+1)=2n_{\rm ph}^{\rm max}(2n_{\rm ph}^{\rm max}+1)$ photon channels, and thus a $1/(2n_{\rm ph}^{\rm max})$ prefactor appears in Eq. (A7) to avoid double counting. Summing over p', Eq. (A7) can be written in a more compact matrix form,

$$\frac{\mathrm{sign}(p)}{2n_{\rm ph}^{\rm max}}\int_{-\infty}^{\infty} dE\,\mathrm{Tr}[\check{G}^r(E)\check{f}(E)\check{\Gamma}(E)\check{G}^a(E)\check{\Gamma}^{(p)}(E) - \check{G}^r(E)\check{\Gamma}(E)\check{G}^a(E)\check{f}^{(p)}(E)\check{\Gamma}^{(p)}(E)],$$

which recovers the expression Eq. (27) shown in Ref. 50.

*d92222006@ntu.edu.tw
†crchang@phys.ntu.edu.tw

[1]S. A. Wolf, D. D. Awschalom, R. A. Buhrman, J. M. Daughton, S. von Molnár, M. L. Roukes, A. Y. Chtchelkanova, and D. M. Treger, Science **294**, 1488 (2001).
[2]I. Žutić, J. Fabian, and S. Das Sarma, Rev. Mod. Phys. **76**, 323 (2004).
[3]J. Fabian, A. Matos-Abiaguea, C. Ertlera, P. Stano, and I. Žutić, Acta Physica Slovaca **57**, 565 (2007).
[4]D. D. Awschalom and M. E. Flatté, Nat. Phys. **3**, 153 (2007).
[5]I. Adagideli, G. E. W. Bauer, and B. I. Halperin, Phys. Rev. Lett. **97**, 256601 (2006).
[6]M. I. D'yakonov and V. I. Perel', Phys. Lett. A **35**, 459 (1971).
[7]J. E. Hirsch, Phys. Rev. Lett. **83**, 1834 (1999).
[8]S. Murakami, N. Nagaosa, and S.-C. Zhang, Science **301**, 1348 (2003).
[9]J. Sinova, D. Culcer, Q. Niu, N. A. Sinitsyn, T. Jungwirth, and A. H. MacDonald, Phys. Rev. Lett. **92**, 126603 (2004).
[10]E. M. Hankiewicz, J. Li, T. Jungwirth, Q. Niu, S.-Q. Shen, and J. Sinova, Phys. Rev. B **72**, 155305 (2005).
[11]E. Saitoh, M. Ueda, H. Miyajima, and G. Tatara, Appl. Phys. Lett. **88**, 182509 (2006).
[12]O. Mosendz, J. E. Pearson, F. Y. Fradin, G. E. W. Bauer, S. D. Bader, and A. Hoffmann, Phys. Rev. Lett. **104**, 046601 (2010).
[13]S. O. Valenzuela and M. Tinkham, Nature (London) **442**, 176 (2006).
[14]L. K. Werake, B. A. Ruzicka, and H. Zhao, Phys. Rev. Lett. **106**, 107205 (2011).
[15]Y. Tserkovnyak, A. Brataas, G. E. W. Bauer, and B. I. Halperin, Rev. Mod. Phys. **77**, 1375 (2005).
[16]K. Uchida, T. Ota, H. Adachi, J. Xiao, T. Nonaka, Y. Kajiwara, G. E. W. Bauer, S. Maekawa, and E. Saitoh, J. Appl. Phys. **111**, 103903 (2012).
[17]K. Ando, S. Takahashi, J. Ieda, H. Kurebayashi, T. Trypiniotis, C. H. W. Barnes, S. Maekawa, and E. Saitoh, Nat. Mater. **10**, 655 (2011).
[18]E. I. Rashba, Phys. Rev. B **62**, 16267 (2000).
[19]J. Ohe, A. Takeuchi, G. Tatara, and B. Kramer, Physica E **40**, 1554 (2008).
[20]A. Takeuchi, K. Hosono, and G. Tatara, Phys. Rev. B **81**, 144405 (2010).
[21]R. H. Silsbee, A. Janossy, and P. Monod, Phys. Rev. B **19**, 4382 (1979).
[22]P. W. Brouwer, Phys. Rev. B **58**, R10135 (1998).
[23]Y. Aharonov and A. Casher, Phys. Rev. Lett. **53**, 319 (1984).
[24]H. Mathur and A. D. Stone, Phys. Rev. Lett. **68**, 2964 (1992).
[25]K. Richter, Physics **5**, 22 (2012).
[26]Y. Aharonov and J. Anandan, Phys. Rev. Lett. **58**, 1593 (1987).
[27]D. Frustaglia and K. Richter, Phys. Rev. B **69**, 235310 (2004).
[28]F. Nagasawa, J. Takagi, Y. Kunihashi, M. Kohda, and J. Nitta, Phys. Rev. Lett. **108**, 086801 (2012).
[29]J. Nitta, T. Akazaki, H. Takayanagi, and T. Enoki, Phys. Rev. Lett. **78**, 1335 (1997).
[30]D. Grundler, Phys. Rev. Lett. **84**, 6074 (2000).
[31]M. König, A. Tschetschetkin, E. M. Hankiewicz, J. Sinova, V. Hock, V. Daumer, M. Schafer, C. R. Becker, H. Buhmann, and L. W. Molenkamp, Phys. Rev. Lett. **96**, 076804 (2006).
[32]J. Nitta and T. Bergsten, New J. Phys. **9**, 341 (2007).
[33]B. Molnar, F. M. Peeters, and P. Vasilopoulos, Phys. Rev. B **69**, 155335 (2004).
[34]S. Souma and B. K. Nikolić, Phys. Rev. B **70**, 195346 (2004).
[35]S. Souma and B. K. Nikolić, Phys. Rev. Lett. **94**, 106602 (2005).
[36]Y. Tserkovnyak and A. Brataas, Phys. Rev. B **76**, 155326 (2007).
[37]M. F. Borunda, X. Liu, A. A. Kovalev, X.-J. Liu, T. Jungwirth, and J. Sinova, Phys. Rev. B **78**, 245315 (2008).
[38]N. Tsuji, T. Oka, and H. Aoki, Phys. Rev. B **78**, 235124 (2008).
[39]B. K. Nikolić and S. Souma, Phys. Rev. B **71**, 195328 (2005).
[40]D. F. Martinez, J. Phys. A **36**, 9827 (2003).
[41]T. Kitagawa, T. Oka, A. Brataas, L. Fu, and E. Demler, Phys. Rev. B **84**, 235108 (2011).
[42]K. Y. Wang, K. W. Edmonds, R. P. Campion, L. X. Zhao, A. C. Neumann, C. T. Foxon, B. L. Gallagher, and P. C. Main, in *Physics of Semiconductors 2002: Proceedings of the 26th International Conference on the Physics of Semiconductors held in Edinburgh, UK, 29 July-2 August 2002*, edited by A. R. Long and J. H. Davies (IOP Publishing, Bristol, 2003), Vol. 171 of Inst. Phys. Conf. Ser., p. 58.
[43]K. Hattori, J. Phys. Soc. Jpn. **77**, 034707 (2008).
[44]S.-H. Chen and C.-R. Chang, Phys. Rev. B **77**, 045324 (2008).
[45]M.-H. Liu, J.-S. Wu, S.-H. Chen, and C.-R. Chang, Phys. Rev. B **84**, 085307 (2011).
[46]P. Zhang, Q.-K. Xue, and X. C. Xie, Phys. Rev. Lett. **91**, 196602 (2003).
[47]K. Hattori, Phys. Rev. B **75**, 205302 (2007).
[48]Y. Tserkovnyak, T. Moriyama, and J. Q. Xiao, Phys. Rev. B **78**, 020401(R) (2008).
[49]S.-H. Chen, C.-R. Chang, J. Q. Xiao, and B. K. Nikolić, Phys. Rev. B **79**, 054424 (2009).
[50]F. Mahfouzi, J. Fabian, N. Nagaosa, and B. K. Nikolić, Phys. Rev. B **85**, 054406 (2012).
[51]M. Moskalets and M. Büttiker, Phys. Rev. B **66**, 205320 (2002).
[52]B. H. Wu and J. C. Cao, Phys. Rev. B **73**, 245412 (2006).
[53]L. Arrachea, Phys. Rev. B **72**, 125349 (2005).
[54]L. E. F. Foa Torres, Phys. Rev. B **72**, 245339 (2005).
[55]B. H. Wu and J. C. Cao, J. Phys.: Condens. Matter **20**, 085224 (2008).
[56]B. H. Wu and J. C. Cao, Phys. Rev. B **81**, 085327 (2010).
[57]B. H. Wu and C. Timm, Phys. Rev. B **81**, 075309 (2010).
[58]M. G. Floquet, Ann. Sci. Ec. Normale Super. **12**, 47 (1883).
[59]H. Haug and A.-P. Jauho, *Quantum Kinetics in Transport and Optics of Semiconductors* (Springer, Berlin, 2007).
[60]E. I. Rashba, Fizika tverd. tela **2**, 1224 (1960) [Sov. Phys. Solid State **2**, 1109 (1960)].
[61]P. W. Anderson, Phys. Rev. **124**, 41 (1961).
[62]G. Grosso and G. P. Parravicini, *Solid State Physics* (Academic Press, New York, 2000), Chap. XVI, Sec. 5.
[63]M. G. Vavilov, V. Ambegaokar, and I. L. Aleiner, Phys. Rev. B **63**, 195313 (2001).
[64]V. I. Yudson, E. Kanzieper, and V. E. Kravtsov, Phys. Rev. B **64**, 045310 (2001).
[65]M. Moskalets and M. Büttiker, Phys. Rev. B **66**, 035306 (2002).
[66]M. L. Polianski, M. G. Vavilov, and P. W. Brouwer, Phys. Rev. B **65**, 245314 (2002).
[67]B. Wang and J. Wang, Phys. Rev. B **66**, 125310 (2002).
[68]B. Wang and J. Wang, Phys. Rev. B **66**, 201305 (2002).
[69]B. Wang, J. Wang, and H. Guo, Phys. Rev. B **68**, 155326 (2003).
[70]S. Kohler, J. Lehmann, and P. Hänggi, Phys. Rep. **406**, 379 (2005).
[71]C. Li, Y. Yu, Y. Wei, and J. Wang, Phys. Rev. B **75**, 035312 (2007).